Metamaterials and their applications towards novel imaging technologies

Author: Claire Watts

Boston College

The Graduate School of Arts and Sciences

Department of Physics

METAMATERIALS AND THEIR APPLICATIONS TOWARDS NOVEL IMAGING TECHNOLOGIES

a dissertation

by

CLAIRE M. WATTS

submitted in partial fulfillment of the requirements

for the degree of

Doctor of Philosophy

August 2015

Metamaterials and Their Applications Towards Novel Imaging Technologies

Claire M. Watts

Boston College, Graduate School of Arts and Sciences, Spring 2015

Graduate Advisor: Willie J. Padilla

Abstract

This thesis will describe the implementation of novel imaging applications with electromagnetic metamaterials. Metamaterials have proven to be host to a multitude of interesting physical phenomena and give rich insight electromagnetic theory. This thesis will explore not only the physical theory that give them their interesting electromagnetic properties, but also the many applications of metamaterials.

There is a strong need for efficient, low cost imaging solutions, specifically in the longer wavelength regime. While this technology has often been at a standstill due to the lack of natural materials that can effectively operate at these wavelengths, metamaterials have revolutionized the creation of devices to fit these needs. Their scalability has allowed them to access regimes of the electromagnetic spectrum previously unobtainable with natural materials. Along with metamaterials, mathematical techniques can be utilized to make these imaging systems streamlined and effective.

Chapter 1 gives a background not only to metamaterials, but also details several parts of general electromagnetic theory that are important for the understanding of metamaterial theory. Chapter 2 discusses one of the most ubiquitous types of metamaterials, the metamaterial absorber, examining not only its physical mechanism, but also its role in metamaterial devices. Chapter 3 gives a theoretical background of imaging at longer wavelengths, specifically single pixel

imaging. Chapter 3 also discusses the theory of Compressive Sensing, a mathematical construct that has allowed sampling rates that can exceed the Nyquist Limit. Chapter 4 discusses work that utilizes photoexcitation of a semiconductor to modulate THz radiation. These physical methods were used to create a dynamic THz spatial light modulator and implemented in a single pixel imaging system in the THz regime. Chapter 5 examines active metamaterial modulation through depletion of carriers in a doped semiconductor via application of a bias voltage and its implementation into a similar single pixel imaging system. Additionally, novel techniques are used to access masks generally unobtainable by traditional single pixel imagers. Chapter 6 discusses a completely novel way to encode spatial masks in frequency, rather than time, to create a completely passive millimeter wave imager. Chapter 7 details the use of telecommunication techniques in a novel way to reduce image acquisition time and further streamline the THz single pixel imager. Finally, Chapter 8 will discuss some future outlooks and draw some conclusions from the work that has been done.

Acknowledgements

This dissertation is a result of incredible support, patience, and encouragement from so many people. Without the colleagues, friends, and family in my life, I would be nowhere near where I am today.

Firstly, I would like to thank my advisor, Professor Willie Padilla. Five years ago, Willie decided to take a chance on me and hire me for research before I started graduate school at BC. Little did I know that this single event would have a huge impact on the rest of my life. Throughout the years doing research with Willie, I have learned more than I could possibly imagine. Willie challenged me to work my hardest and strive for greatness in the field.

Working in the Padilla Lab every day was such a pleasure. My fellow members of the Padilla Lab provided amazing support and knowledge. I would specifically like to mention Chris Bingham, Dr. David Shrekenhamer, Dr. Xianliang Liu, Dr. Wenchen Chen, Dr. Kebin Fan, Christian Nadell, Xinyu Liu, Xueyuan Wu, Paul Weinand, Michelle Cunningham, Nick Caira, Mike Boyarsky, and Tim Sleasman.

Many of my projects would not have been possible without support from collaborators. I would like to acknowledge Prof. Brian Tracey, Prof. Eric Miller, and Prof. Sameer Sonkusale from Tufts University, Prof. Sanjay Krishna and Dr. John Montoya in the ECE Dept. at the University of New Mexico, Profs. David Smith and Nan Jokerst in the ECE Dept. at Duke University as well as Prof. Smith's students Guy Lipworth and Dr. John Hunt. Working alongside all of you was truly enriching and I could not have completed my work without your support.

Boston College provided me with such a great environment to be a graduate student. I was constantly learning from my lab-mates, professors in the department, and my fellow graduate students. I would like to thank Prof. Naughton and Prof. Kempa for taking the time to be on my doctoral committee. I would also like to thank Paul Dee and Richard Pijar from the machine shop

as well as Steve Shepard and Greg McMahon from the clean room, who provided some of the most important components to my projects and had seemingly endless patience for my requests. I would also like to thank the members of the Physics Department Staff: Jane Carter, Nancy Chevry, Stephanie Zuehlke, Sile Power, and Gisele Byda. Not only are you are the only reason the department can run, but you were such amazing friends over the years, I will never forget you.

My fellow graduate students at Boston College turned work into something I looked forward to every day. I will never forget our movie nights, beer-thirtys, and happy hours. I specifically want to mention Tom Hogan, who was my best friend in graduate school since the beginning. He and I got each other through countless problem sets and a hell of a summer studying for the qualifiers. I am so lucky that I have him in my life and I can't wait to see him marry his beautiful and wonderful future wife, Laura.

I would like to thank my friends for the constant support they have given me throughout my years in graduate school. I made friends in Boston that I will absolutely never forget and I had some of the best times of my life in our grubby Allston apartments. My Seattle friends stuck by me when I moved out to the East Coast and continued to be a connection to home.

Finally, I want to thank my family. Without their support and love, none of what I did in graduate school would be possible. They suffered through many missed birthdays, late night phone calls, and me being generally stressed for five years. They were calm, patient, supportive, forgiving, helpful, and loving. To my parents, Mary and Bill, my sisters and their husbands, Kate, Caleb, Lauren, and Britt - thank you for everything.

Table of Contents

List of Figures

List of Tables

1. Introduction and Background Information

1.1 Introduction

Electromagnetic metamaterials (EM MMs) are composite structures of subwavelength elements that can be designed to interact with light in specific ways. Their optical characteristics are determined through the geometry of the constituent elements. As such, they are completely scalable and have been demonstrated across much of the electromagnetic spectrum and used for a multitude of applications. This includes use as efficient devices in imaging systems, specifically at long wavelengths. As this thesis will show, metamaterials are a viable option for devices that can operate in real-world products. Additionally, metamaterials give a strong physical insight into electromagnetic theory.

1.2 Electromagnetic Theory

1.2.1 Maxwell's Equations

Before discussing the physics behind metamaterials, it is first pertinent to give a brief overview of electromagnetic theory. We start with Maxwell's equations, which form the basis of all light-matter interactions. These equations were actually developed by several physicists over the course of the early 19th century and were made cohesive by James Clerk Maxwell in 1865 [1]. While Maxwell's equations come in many forms, here we write them for a linear, isotropic media with an absence of any free charges or currents:

$$\bar{\nabla} \cdot \bar{D} = 0 \tag{1.1}$$

$$\bar{\nabla} \cdot \bar{B} = 0 \tag{1.2}$$

$$\bar{\nabla} \times \bar{E} = -\frac{\partial \bar{B}}{\partial t} \tag{1.3}$$

$$\bar{\nabla} \times \bar{H} = \frac{\partial \bar{D}}{\partial t} \tag{1.4}$$

where $\bar{E}$ and $\bar{B}$ are, respectively, the electric and magnetic fields while $\bar{D}$ is the electric displacement, and $\bar{H}$ is the magnetic field strength [2]. This proves useful for sinusoidal oscillating EM waves:

$$\begin{bmatrix}\bar{E}(\bar{r},t)\\ \bar{B}(\bar{r},t)\end{bmatrix} = \begin{bmatrix}\bar{E}_0\\ \bar{B}_0\end{bmatrix} e^{i(\bar{k}\cdot\bar{r}-\omega t)}. \tag{1.5}$$

Plugging this form of the EM wave into Maxwell's equations, we are left with the relationship that $\bar{E}$ and $\bar{B}$ are not only mutually perpendicular, but also perpendicular to the wavevector $\bar{k}$; i.e. we are dealing with a transverse electromagnetic wave with wavevector $\bar{k}$ and angular frequency ω[2].

Here, we have used a form of the constituent relations that provide a connection between incident fields and the corresponding polarization ($\bar{P}$) and magnetization ($\bar{M}$):

$$\bar{D} = \varepsilon_0\bar{E} + \bar{P} = \varepsilon_0(1+\chi_e)\bar{E} = \varepsilon_r\varepsilon_0\bar{E} = \varepsilon\bar{E}, \tag{1.6}$$

$$\bar{B} = \mu_0(\bar{H} + \bar{M}) = \mu_0(1+\chi_m)\bar{H} = \mu_r\mu_0\bar{H} = \mu\bar{H}. \tag{1.7}$$

Several characteristic optical constants of the media have been defined in these statements: the magnetic and electric susceptibility (χ_e and χ_m), the electric permittivity – free space, absolute, and relative ($\varepsilon_0, \varepsilon, \varepsilon_r$), and the magnetic permeability – free space, absolute, and relative (μ_0, μ, μ_r) [2]. In general, these will all be complex and dispersive (functions of frequency), i.e. $\varepsilon = \tilde{\varepsilon}(\omega) = \varepsilon_1(\omega) + i\varepsilon_2(\omega)$ and $\mu = \tilde{\mu}(\omega) = \mu_1(\omega) + i\mu_2(\omega)$. In going further, the frequency dependence and complex nature of the parameters will not always be explicitly stated. We can define additional material parameters using the permittivity and the permeability: the index of refraction (n), the wave impedance (Z), and the conductivity (σ):

$$n = \sqrt{\varepsilon_r\mu_r}, \tag{1.8}$$

$$Z = \sqrt{\mu/\varepsilon}, \tag{1.9}$$

$$\text{and } \sigma = i\omega(\varepsilon_0 - \varepsilon), \tag{1.10}$$

where all these parameters have the implied real and imaginary components as well as frequency dependence.

1.2.2 Characteristics of a Wave Traveling Through a Medium

The combination of Maxwell's equations and the constitutive relations provide a connection between how charges interact with dynamic fields on a microscopic level, and optical parameters that we associate with media on a macroscopic level, such as ε and μ. In addition, by substituting the general form for an oscillating EM wave (1.5) into Maxwell's equations (1.1 - 1.4), we derive several other properties about the EM traveling through the medium. For example, we write the dispersion relation between the wavevector $\bar{k}$ and the angular frequency ω:

$$k^2 = \omega^2 \varepsilon \mu. \tag{1.11}$$

Relating this to the velocity of the EM wave moving through the media, we see that the speed of light is reduced by a factor of n:

$$v = {}^{c}/_{n}. \tag{1.12}$$

If the EM wave is comprised of several different wavevectors, each phase front will have its own velocity:

$$v_p = {}^{\omega}/_{k}, \tag{1.13}$$

known as the phase velocity. The wave packet as a whole will travel with speed defined as the group velocity:

$$v_g = {}^{d\omega}/_{dk}. \tag{1.14}$$

It should be noted that for dispersive media, different spectral components will travel at different speeds and hence acquire a phase difference; this generally results in distortion of the wavepacket [2].

1.2.3 Constituent Relations

For the above discussion, we assumed several things about the media. Namely, that it was linear and had simple relations between the displacement fields and incident fields based on ε and

μ. In reality, the displacement fields are coupled in a much more complicated way. Very generally, we can write:

$$\begin{bmatrix}\bar{D}\\ \bar{B}\end{bmatrix} = \begin{bmatrix}\bar{\bar{\varepsilon}} & \bar{\bar{\xi}}\\ \bar{\bar{\zeta}} & \bar{\bar{\mu}}\end{bmatrix} \cdot \begin{bmatrix}\bar{E}\\ \bar{H}\end{bmatrix}, \tag{1.15}$$

where the double bar notation represents that each one of these optical constants is a tensor carrying wavevector dependence:

$$\bar{\bar{\varepsilon}} = \begin{bmatrix}\varepsilon_{xx} & \varepsilon_{xy} & \varepsilon_{xz}\\ \varepsilon_{yx} & \varepsilon_{yy} & \varepsilon_{yz}\\ \varepsilon_{zx} & \varepsilon_{zy} & \varepsilon_{zz}\end{bmatrix}[3]. \tag{1.16}$$

The constants $\bar{\bar{\xi}}$ and $\bar{\bar{\zeta}}$ describe coupling between the electric and magnetic responses and are known as magneto-optical permittivities.

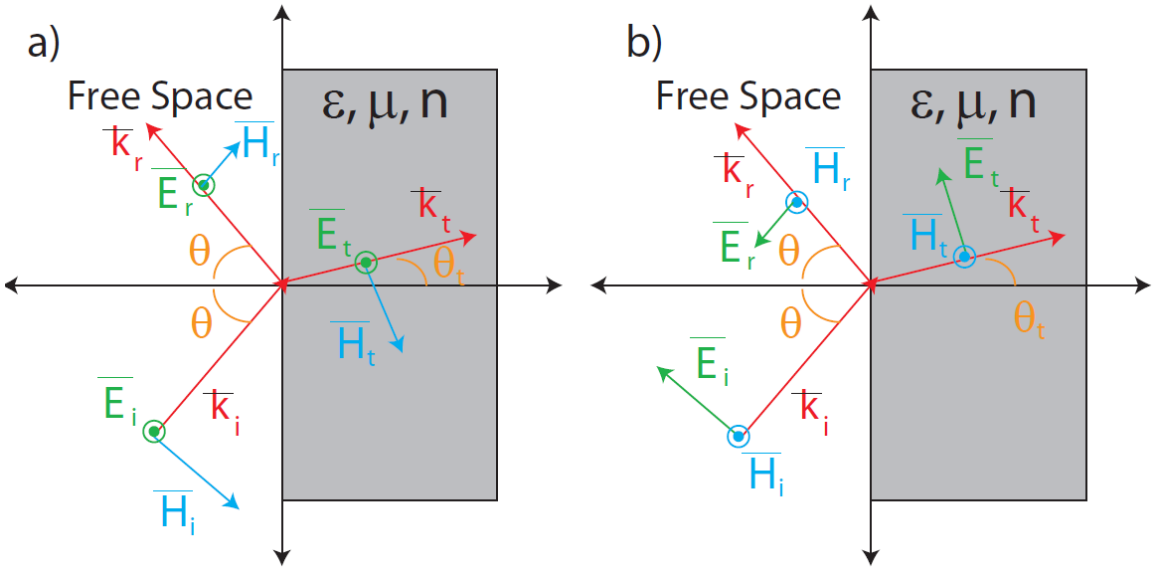

Fig. 1.1 – EM Wave Propagation through an Interface Schematic of an incident electromagnetic wave on a planar interface for (a) TE and (b) TM polarized wave. Light is incident from the left from free space ($\bar{k}_i$) at some angle of incidence (θ) and reflects at the same angle ($\bar{k}_r$). The light transmits ($\bar{k}_t$) through the interface at some angle θ_t and enters the medium with parameters n, ε, μ.

1.2.4 Fresnel's Equations

While the above relations are useful in providing a connection between the motion of charges on a microscopic level and optical parameters that we associate with macroscopic media,

we still hope to connect these to quantities that are measured experimentally, such as transmission ($T(\omega)$) and reflection ($R(\omega)$). To do this, we must take into account the dynamics of light crossing from one media to another with different optical parameters, resulting in Fresnel's equations. In Fig. 1.1 the wave travels left to right, from free space to some medium with optical constants n, ε, and, μ (shaded region) for both TE and TM polarizations. The reflection off the interface and transmission through the interface are:

$$R_{TE} = \left|\frac{\cos\theta - (\mu_r)^{-1}\sqrt{n^2 - \sin^2\theta}}{\cos\theta + (\mu_r)^{-1}\sqrt{n^2 - \sin^2\theta}}\right|^2, R_{TM} = \left|\frac{\varepsilon_r \cos\theta - \sqrt{n^2 - \sin^2\theta}}{\varepsilon_r \cos\theta + \sqrt{n^2 - \sin^2\theta}}\right|^2 \text{and} \quad (1.17)$$

$$T_{TE} = \left|\frac{2\cos\theta}{\cos\theta + (\mu_r)^{-1}\sqrt{n^2 - \sin^2\theta}}\right|^2 \left(\frac{\varepsilon_r \cos\theta_t}{n\cos\theta}\right), T_{TM} = \left|\frac{2n\cos\theta}{\varepsilon_r \cos\theta + \sqrt{n^2 - \sin^2\theta}}\right|^2 \left(\frac{\varepsilon \cos\theta_t}{n\cos\theta}\right) [2].$$

(1.18)

1.2.5 Optical Constants and the Drude-Lorentz Model

Although we have given a comprehensive relationship between light and matter in terms of the media's optical parameters, we have yet to touch on why media interacts with light the way it does. We start again with a microscopic description of the motion of an electron acting as an oscillator with some spring constant $m{\omega_0}^2$ in an electric field governed by Newton's 2nd law:

$$m[\ddot{\bar{r}} + \gamma\dot{\bar{r}} + {\omega_0}^2\bar{r}] = -e\bar{E}(\bar{r}, t)[2], \quad (1.19)$$

with $\bar{r}$ representing the electron displacement, e and m representing the electron charge and mass, ω_0 denoting the resonant frequency, and γ representing a damping factor. Note, we have ignored force from the magnetic field, with the assumption that the amplitude of the magnetic field is small compared the electric field and any subsequent motion will not greatly displace the electron. Using the plane wave form of the electric field, we can solve for the position and hence the polarization of the electron:

$$\bar{p} = -e\bar{r} = \frac{e^2}{m}({\omega_0}^2 - \omega^2 - i\omega\gamma)\bar{E}\ [2]. \quad (1.20)$$

Recalling the relationship between the incident electric field and the electron polarization (Eq. 1.6), we can solve for the dielectric constant. Assuming there are N molecules per unit volume

with Z electrons per molecule, each with various damping coefficients $\gamma_j$and resonant frequencies ω_j, we can sum the responses to solve for the dielectric function, known as the Drude-Lorentz equation:

$$\varepsilon_r(\omega) = 1 + \sum_j f_j\left({\omega_0}^2 - \omega^2 - i\omega\gamma_j\right)^{-1}. \quad (1.21)$$

Here we assume that the oscillator strengths f_j follow the sum rule: $Z = \sum_j f_j$ [2].

We have now laid the groundwork for the interaction between electromagnetic waves and media with defined optical constants such as $\varepsilon(\omega)$ and $\mu(\omega)$. Metamaterials have tunable optical constants through their geometry, allowing their interactions with light, such as transmission, reflection, phase, etc. to be designed by the user. In the next section we will discuss how the subwavelength constituents of metamaterials act collectively to give an effective optical response. Additionally, metamaterials have a strong analog to atoms in a lattice through their resonant nature, often giving a Lorentzian-style permittivity or permeability.

1.3 Metamaterial Theory

1.3.1 Introduction to Metamaterials

Metamaterials are designer electromagnetic materials comprised of subwavelength elements with effective optical constants, the electric permittivity $\varepsilon(\omega)$ and the magnetic permeability $\mu(\omega)$, determined by the geometry of their constituents. Generally, they are comprised of unit cells, each on the order of $\lambda/10$ or often smaller, patterned in a large array. As each unit cell is much smaller than the operation wavelength of light, electromagnetic waves interact with metamaterials as an effective medium defined by optical constants, rather than diffracting off the individual elements. One can define an effective electric permittivity and magnetic permeability, $\varepsilon_{eff}(\omega)$ and $\mu_{eff}(\omega)$, respectively.

The effective optical constants of metamaterials are largely influenced by the geometry of the unit cells, rather than their band structure or chemistry, as in normal materials. This has the

exciting result that metamaterials are scalable across much of the electromagnetic spectrum, and have been demonstrated to have responses from radio frequencies [4] all the way into the optical and visible regimes [5].

Metamaterials were not the first effective media to utilize artificial elements to achieve specific EM responses. In fact, as early as 1898, Jagadis Chunder Bose utilized twisted copper wires in a microwave experiment studying polarization [6]. The notion of artificial dielectrics truly took off in the 1940's with work done at Bell Labs, specifically Kock's metallic delay lens [7] and continued throughout the century. Additionally, artificial magnetism, or magnetism achieved without magnetic components, has similarly timed origins and can be found in a classical antenna textbook [8]. Artificial plasmas, or artificially engineered media with negative $\varepsilon(\omega)$, have been known since the 1960's [9, 10].

However, most consider the "birth" of metamaterials to be the introduction of John Pendry's artificial magnetism in 1999 [11] along with the seminal paper numerically studying the first structure with simultaneously negative $\varepsilon(\omega)$ and $\mu(\omega)$ [12]. These publications introduced a paradigm shift that allowed for artificial materials, later termed metamaterials by Walser [13], to achieve more exotic properties over a larger range of the EM spectrum, specifically into much shorter wavelengths, than their predecessors.

The introduction of a negative index material (NIM), or a material that's simultaneously negative values of $\varepsilon_{eff}(\omega)$ and $\mu_{eff}(\omega)$ caused it to have an index of refraction, $n_{eff}(\omega) < 0$, by Smith in 2000 was a very exciting step for metamaterials. Since then, metamaterials have been shown to achieve a multitude of properties such as tailored absorption [14] and emission [15], multi-band response [16], or even dynamic performance [17], across a large bandwidth of the electromagnetic spectrum. The total design flexibility has allowed metamaterials to be seamlessly made into a multitude of devices, such as super lenses [18], invisibility cloaks [19], and spatial light modulators [20].

1.3.2 Negative Index Materials

In 1999, John Pendry released a study of a magnetic material comprised from non-magnetic resonant elements [11]. These structures have a tunable magnetic response, so while most natural materials were confined to interact strongly with magnetic fields at low frequencies, Pendry was able to tune the response to higher frequencies. Of the many magnetic metamaterials proposed by Pendry, the one with the most traction in the field was the double split ring resonator (dSRR), shown in Fig. 1.2(a), which gave a frequency band of negative $\mu_{eff}(\omega)$ in the microwave regime.

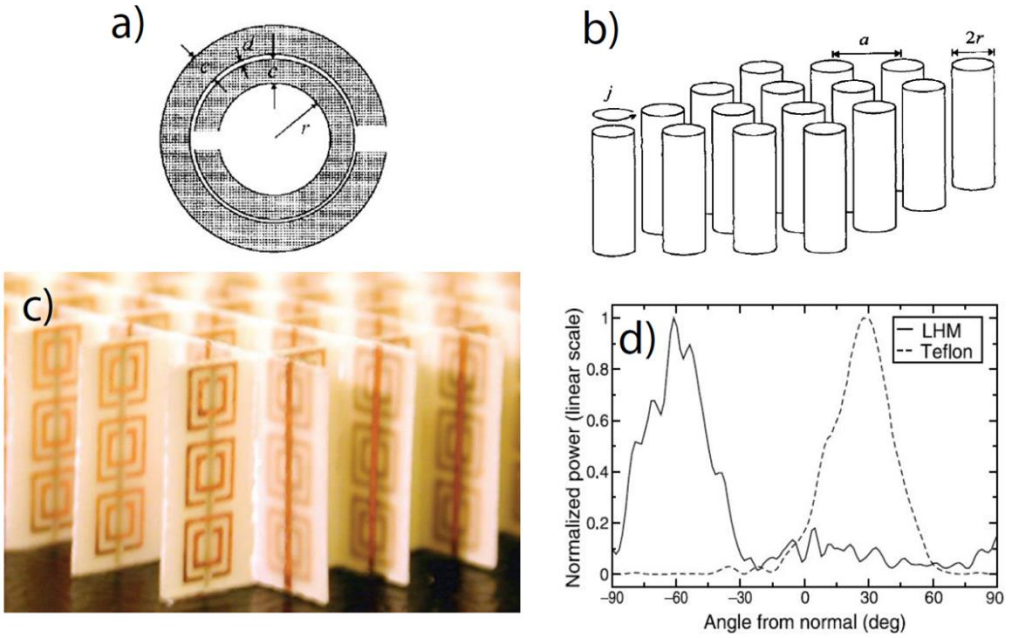

Fig. 1.2 – Negative Index Material, Experimental Demonstration Component of experimentally demonstrated negative index material. (a) Array of metallic wires. (b) Double split ring resonator. (Pendry, 1999) (c) Composite structure shown to exhibit a negative index of refraction. (d) Experimental angular transmission spectra showing negative refraction (Shelby, 2001).

This was particularly exciting because it opened up the possibility for a NIM. While some work existed on backwards waves and NIM [21], it wasn't until 1968 that a methodical analysis was done. Russian physicist Victor Veselago postulated that a material with simultaneous negative ε and μ would have exotic properties such as opposite phase and group velocity, inversion of the Doppler shift, and a reversal of Snell's Law [22]. While negative ε

materials are common, i.e. any metal above the plasma frequency, negative μ materials are quite rare and do not exist in frequency regimes accessible by negative ε materials [23].

Pendry proposed an array of thin wires (Fig. 1.2(b)) that acted as a dilute plasma, shifting the plasma frequency to the microwave region. Hence, through the use of these artificial materials, components were found that had simultaneous frequency regimes of negative $\varepsilon_{eff}(\omega)$ and $\mu_{eff}(\omega)$.

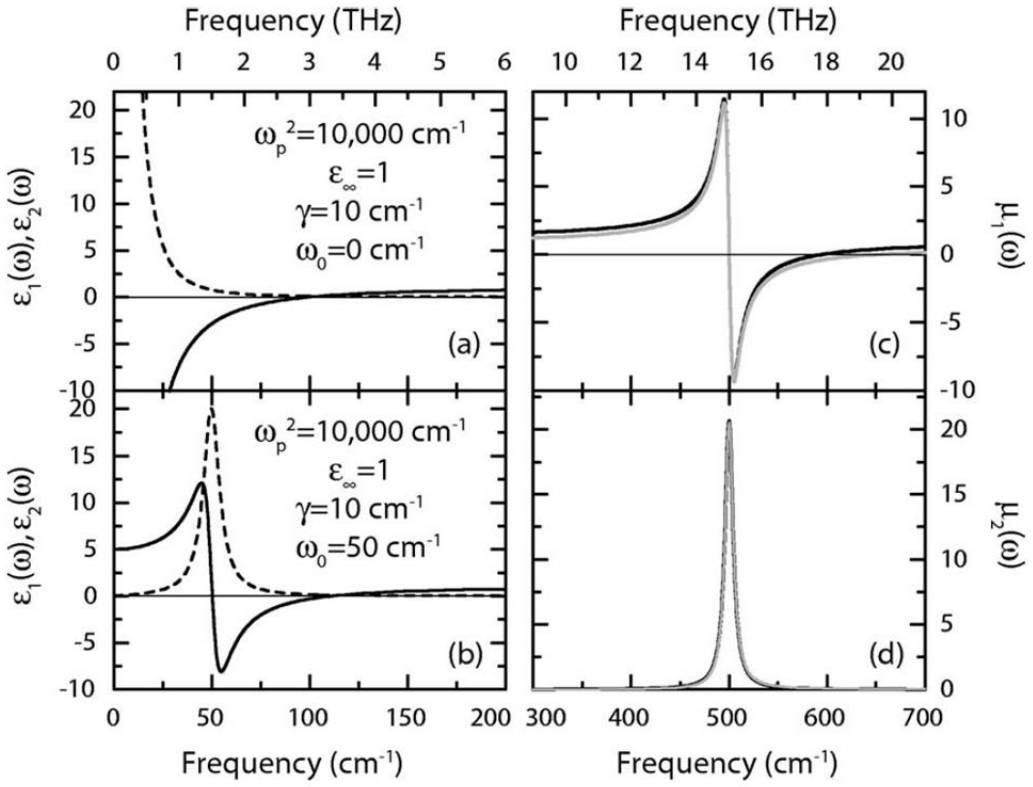

Fig. 1.3 – Drude-Lorentz Model for Several MM Unit Cells Real (solid) and imaginary (dotted) components of optical constants for several Lorentz oscillators. (a) $\boldsymbol{\varepsilon(\omega)}$ for the Drude model (i.e. $\boldsymbol{\omega_0 = 0}$). (b) $\boldsymbol{\varepsilon(\omega)}$ for a Lorentz oscillator. (c) $\boldsymbol{\mu(\omega)}$ for both versions of the magnetic permeability given. Grey denotes Eq. 1.22, black denotes Eq. 1.23. (Padilla, 2006)

In 2000, David Smith and colleagues experimentally demonstrated such a negative index material by combining these two types of constituent elements, an array of thin copper wires to achieve a negative $\varepsilon_{eff}(\omega)$ and an array of dSRRs to achieve a negative $\mu_{eff}(\omega)$ [12]. In 2001, reversal of Snell's Law was shown in a metamaterial prism with $n_{eff} = -2.7$ [24]. Their composite structure and results are shown in Fig. 1.2(c) and (d).

1.3.3 Metamaterials as an Effective Medium

The effective optical characteristics of metamaterials that give them their often exotic responses to light (such as negative index of refraction) are dependent upon the geometric parameters of the unit cells. The same way we described the Lorentzian model in Section 1.2, where each atom is treated as an oscillator in a driving field, we can consider metamaterial unit cells to be artificial "atoms" with similar properties such as a resonant frequency ω_0, filling fraction F, and some damping constant γ. For example, Pendry derived the effective permittivity for an array of dSRRs to be:

$$\mu_r(\omega) = 1 + F\frac{\omega^2}{{\omega_0}^2-\omega^2-i\gamma\omega} \text{ [11].} \tag{1.22}$$

However, in order to preserve causality, it is often common to see the effective permittivity written as the Drude-Lorentz equation (Eq. 1.21):

$$\mu_r(\omega) = 1 + \frac{{\omega_{mp}}^2}{{\omega_0}^2-\omega^2-i\gamma\omega}, \tag{1.23}$$

where ω_{mp} is the magnetic plasma frequency [25]. The Drude-Lorentzian parameters, ω_{mp}, ω_0, and γ can all be determined by the characteristics of the MM unit cell.

To achieve the electric response, Pendry and then Smith used an array of infinite thin metallic wires, in essence acting like a dilute plasma [11, 12]. Again, starting with the Drude-Lorentz model given in Eq. 1.21, we can replace the resonance frequency $\omega_0 = 0$ as to represent the Drude model. The plasma frequency was solved as a function of several geometric parameters:

$$\varepsilon_r(\omega) = 1 - \frac{{\omega_p}^2}{\omega^2+i\gamma\omega}, \tag{1.24}$$

$${\omega_p}^2 = {2\pi c^2}/{a^2 \ln(a/r)} \tag{1.25}$$

with the parameters a and r representing the periodicity and radius of the metallic wires, respectively.

With the correct polarization, a double SRR can give a purely magnetic response. However, it is also useful to have access to a purely electric response. This can be achieved with a structure known as an electric ring resonator (ERR), where the symmetric rings are used to cancel any magnetic effect. This will then give an electric permittivity with the familiar Drude-Lorentz form:

$$\varepsilon_r(\omega) = 1 + \frac{{\omega_p}^2}{{\omega_0}^2 - \omega^2 - i\gamma\omega}. \tag{1.26}$$

The effective optical constants for the structures listed above are plotted in Fig. 1.3.

1.4 A Review of Metamaterials

We have shown in the past section that metamaterials, through simply their geometry, can not only obtain optical properties not seen in nature, but have a design-ability that makes them useful for a multitude of purposes. Below we give a short survey of some types of metamaterials, as well as the current state of the art for design and simulation, fabrication, and characterization.

1.4.1 Metamaterial Building Blocks

While we have discussed various types of metamaterial unit cells, i.e. the dSRR, the wire array, and the ERR, there exist many other types of unit cells that exhibit various properties and interact with light in different ways. Other than the choice to have either a magnetic or electric response, or a combination of both, filling fraction is also an important point to consider. It is often useful to have a high filling fraction and thus have the unit cells be very subwavelength, as demonstrated in a RF spiral metamaterial, which achieves a periodicity of $\sim\lambda/700$ [26]. Alternatively, as we move towards higher frequencies, the metamaterial structures themselves must become smaller to retain their effective medium response. Due to fabrication constraints (discussed in more detail below), these structures often become simpler, trading complex ERR shapes for simpler resonators.

Metamaterials have been developed to operate for numerous types of electromagnetic functions. They can be made extremely narrowband [27], broad or multi-band [16], operate at a multitude of input angles [28], input polarizations [29], and have even been fabricated on flexible substrates [30].

1.4.2 Metamaterial Absorbers

The exciting prospect of negative index materials spurred a great deal of research for MMs in the early 2000's. It was soon realized that metamaterials could move beyond negative index, and in fact could be tuned and optimized for many desired electromagnetic properties in an arbitrary frequency regime.

Possibly one of the most ubiquitous types of metamaterials is the metamaterial absorber (MMA). It was first demonstrated in 2008 in the microwave regime where an absorption of 88% was achieved at 11.5 GHz [31]. The basic assembly of an MMA consists of a resonating structure over a ground plane separated by a dielectric layer [14]. This has been demonstrated across much of the electromagnetic spectrum, from the microwave to optical regimes and has been utilized in many applications and devices [14]. The physical mechanisms behind the MMA will be discussed further in chapter 2.

1.4.3 Terahertz Metamaterials

Because metamaterials have electromagnetic properties, including their operation wavelength, controlled simply through their geometry, they can easily be scaled across much of the electromagnetic spectrum. The THz regime (300 GHz – 10 THz), or so called "THz – Gap," is notoriously difficult to access, as there is strong atmospheric attenuation across the regime [32]. In addition, there are a general lack of sources, detectors, and modulators that operate as efficiently as their counterparts in the radio-frequency or infrared/optical regimes [33]. However, there are plenty of potential applications for devices that can harness this part of the electromagnetic spectrum, such as security screening [34], all-weather navigation [35], and skin-cancer detection [36]. In 2004, a split ring resonator design was scaled to be subwavelength in the

THz regime (from a periodicity on the order of 10 mm to 36 μm) and was shown to give a strong magnetic response around 1 THz [37]. Without any additional engineering, the structure showed an almost identical response three orders of magnitude higher in frequency than its counterpart, simply by scaling. The power of this design flexibility has allowed the development of THz metamaterial devices such as modulators [38], sensors [39], active spatial masks [20].

1.4.4 Dynamic Metamaterials

Thus far, we have shown that with the appropriate design of the unit cell geometry, a multitude of electromagnetic properties can be realized by metamaterials. However, it would be very beneficial to actively tune the optical properties of metamaterials. This has been achieved in several different ways across the electromagnetic spectrum.

At lower frequencies, it is common to see inclusions of electronically controlled elements such as diodes and varactors into the metamaterial unit cell [40, 41]. As we move to higher frequencies, semiconductors are often used to achieve a dynamically tunable metamaterial. For example, a bias applied to a doped semiconductor will alter its optical properties and, if that semiconductor is included in the MM design, will alter the optical properties of the metamaterial as a whole. This was first demonstrated in 2006 by applying a bias voltage across an n-doped GaAs layer operating as a substrate in a MM design, depleting carriers and changing the metamaterial's effective optical properties (this will be discussed in more detail in chapter 4) [17]. In a similar design, semiconductors can be photodoped using light with energy near the bandgap to modulate MM properties (this also will be discussed in more detail in chapter 5) [42]. Alternatively, one can incorporate phase change material into the metamaterial design, allowing for external control. For example, liquid crystals can be controlled through a bias voltage and have been incorporated into THz MMs [43]. In addition, MEMS metamaterials utilize a mechanical change in the unit cell to achieve a change in the electromagnetic response and have been incorporated in metamaterial design and experimentally demonstrated [44].

1.4.5 Metamaterial Simulation

While the effective optical constant calculations given in Eqs. 1.22 – 1.26 give a simple analysis of how a metamaterial will interact with light, there are often more complicated physical mechanisms at work. Electromagnetic simulation tools are very mature and often allow for a complete and accurate prediction of the way metamaterials will interact with light, permitting complete optimization of the metamaterial design before fabrication. In addition, they can explore some physical phenomena that would be very difficult to attempt analytically, such as interelement coupling, bianisotropy, or power loss density. Some of the most common simulation tools are CST Microwave Studio [45], HFSS [46], and Comsol [47].

Generally, metamaterials are large arrays (much larger than the operation wavelength of light) comprised of identical, subwavelength unit cells. Thus, simulations can be performed easily on one unit cell with the appropriate boundary conditions. In order to best match experimental results, the material properties for the frequency range of interest must be well known. It is often necessary to use frequency dependent models, such as the Drude model for metals in the infrared and optical frequency regimes. The basic process behind these EM simulation tools is to discretize the unit cell and solve Maxwell's Equations for each voxel. Then, complex scattering parameters (S_{11}, S_{21}, S_{12}, and S_{22}) are output to the user. From these scattering parameters, one can extract the effective optical constants of the metamaterial, such as $\varepsilon_{eff}(\omega)$, $\mu_{eff}(\omega)$, and $n_{eff}(\omega)$ [48].

1.4.6 Metamaterial Fabrication

Once the optimal geometric parameters of the metamaterial have been determined, there are a multitude of fabrication methods available that vary depending on the size and complexity of the structure. Typical methods at microwave frequencies, where unit cell sizes are on the order of hundreds of microns or larger, include printed circuit board (PCB) technology [49]. Moving into the THz regime, where the metamaterial periodicity is on the order of tens of microns, PCB techniques no longer become valid. It is more common to see photolithographic methods used in

this case, where metallic and dielectric layers are deposited and patterned [16]. If deep-UV photolithography is used, this method can be pushed to metamaterials operating in the infrared range [15], whose unit cells are on the order of microns. However, it is more common to see serial methods at those wavelengths, such as electron beam lithography [50] and focused ion beam [51]. There are many other types of fabrication methods that exist such as nano-imprint lithography [52] and colloidal nanolithography [53].

While the theory of metamaterials is, indeed, scalable across the electromagnetic spectrum, practical limitations have prevented metamaterials from being realized past the visible range. For example, subwavelength unit cells require features that are difficult to fabricate accurately. In addition, metals can become lossy at higher frequencies, preventing high Q response in metamaterial structures.

1.4.7 Metamaterial Characterization

Much like the fabrication method, the particular characterization technique depends not only on the operation wavelength, but also the specific electromagnetic phenomenon one hopes to measure. At microwave frequencies, vector network analyzers (VNAs) are used to generate and detect both phase and amplitude signal, coupled to free space by horn antennas. Various multipliers, extenders, and filters have extended this technology to the low THz range, although is more commonly seen from the low RF frequencies to the millimeter-wave regimes.

More common in the THz regime is THz time domain spectroscopy, which also gives access to amplitude and phase measurements. A time pulse is used for the sample and reference; a Fourier transform gives information in the frequency domain.

FTIR (Fourier-Transform Infrared) spectroscopy is a bit of a misnomer as it can cover a large part of the electromagnetic spectrum, from THz to visible. The basic idea is to use a Michelson Interferometer to get spectral information from a sample. Current systems allow for different combinations of sources, detectors, and beam splitters as well as the possibility for transmission, reflection, and angular dependent measurements. In addition, FTIR systems can

often be coupled to a microscope with a movable stage, allowing for raster scan microscopy. Additional techniques, such as ellipsometry, optical microscopy, among many others, exist to characterize metamaterials across the EM spectrum.

2. Dual Band Metamaterial Absorber

2.1 Introduction to Metamaterial Absorbers

Now that we have discussed metamaterials in general, we can begin to look at some specific types of metamaterials that make imaging devices possible. In this chapter, we look at one of the most ubiquitous types of MMs in devices, the metamaterial absorber (MM). We detail the design, fabrication, and characterization of a dual banded MMA and explore how its effective characteristics vary spatially. This study can give insight into how to best optimize MM devices, specifically for imaging. We first examine extensively the theoretical background behind MMAs, going into their physical mechanism as EM wave absorbers.

2.1.1 Background and History

The MMA is just one of the many types of electro-magnetic (EM) wave absorbers that has been developed throughout the past century, which all have similar goals: to create a material with simultaneously low transmission and low reflection and hence high absorption. Absorbers have their beginnings in the 1930's [54] but realized their full utility during the 1940's in both improving radar performance and providing concealment against other's radar [54]. Some of the most notable types of absorbers developed and still used today are the Salisbury Screen, the Jaumann absorber, the crossed grating absorber, and circuit analog absorbers. EM wave absorbers have many uses in radar applications, the reduction of electromagnetic interference (EMI), waveguides, and extensive military applications [55 – 60].

As stated in chapter 1, the MMA was first created in 2008 and consisted of a three-layer design operating in the microwave regime of the electromagnetic spectrum [31]. The result was an experimental absorption of 88% at 11.5 GHz [31]. Since the work done in [31], there have been vast developments in the design of the MMA. There now exists absorbers that operate from the microwave to the optical range [49, 61 – 63] with a multitude of characteristics (i.e.

omnidirectional, polarization sensitive or insensitive, broadband, narrowband, or multiband, passive or dynamic) [14]. Metamaterials with multiple responses also inspired a trend in absorbers and now multi-band MMAs operate from the microwave to the optical range [64 – 66].

In this chapter we explore a dual band MMA. By utilizing two differently sized cross structures in a checkerboard array along with a conducting ground plane, our design achieves an impedance match to free space at two wavelengths, 6.25 μm and 8.45 μm. Experimentally, we reach absorptions of up to 89 %. By imaging the dual band metamaterial absorber with different aperture sizes, we are able to clarify the spatial dependence of its optical properties. Additionally, by measuring the effect array size truncation has on the measured absorption, we reveal important information about the effect of nearest-neighbor interaction on the absorption properties. The MM-SLM device, which is utilized for a single pixel imaging system discussed in chapters 5 and 7, has pixels composed of MMAs. With the understanding of the spatial dependence of optical properties of an MMA array, specific in terms of array size, we can optimize our metamaterial device.

2.1.2 MMA Theory

The frequency dependent absorption $A(\omega)$ of a material can be described in terms of the trans-mission $T(\omega)$and the reflection $R(\omega)$ by:

$$A(\omega) = 1 - T(\omega) - R(\omega) \tag{2.1}$$

where we ignore scattering effects and surface electromagnetic waves that lead to a re-radiation of light. Therefore, it is necessary to simultaneously create a frequency band of both low trans-mission and low reflection to maximize absorption. In order to minimize the reflection, the impedance of the metamaterial needs to be matched to free space, with the impedance given by:

$$Z = \sqrt{\frac{\mu}{\varepsilon}} \tag{2.2}$$

where μ and ε are the permeability and the permittivity of the substance, respectively, and $\mu = \mu_0\mu_r$, $\varepsilon = \varepsilon_0\varepsilon_r$. The reflection at normal incidence can be represented by the following equation:

$$R(\omega) = \left|\frac{Z(\omega)-Z_0}{Z(\omega)+Z_0}\right|^2 \quad (2.3)$$

where all parameters depend on the frequency of incident radiation, ω, and the impedance of free space $Z_0 = 120\pi\ \Omega$ [67]. According to Beer's Law, the transmission through a slab approaches

$$T(\omega) = e^{-2n_2 d\omega/c} \quad (2.4)$$

as $Z(\omega)$ approaches Z_0 [68]. In the above equation, n_2 is the complex portion of the index of refraction ($n = n_1 + in_2$), d is the thickness of the slab, ω is the frequency of the incoming light, and c is the speed of light in vacuum. Therefore, if ε and μ are tuned such that $Z = \sqrt{\frac{\mu}{\varepsilon}} = 120\pi\ \Omega$ while simultaneously making $n_2 d \gg c/\omega$, the reflection and transmission would both go to zero, theoretically creating a near unity absorber.

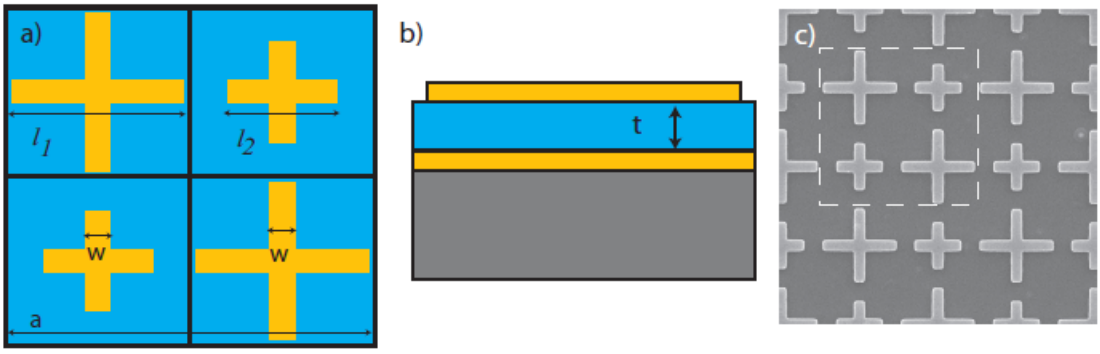

Fig. 2.1 – Dual Band Metamaterial Absorber Schematic Schematic and image of the fabricated metamaterial array. (a) A top view schematic of the two metamaterial absorbers; l_1 = 3.2 µm, l_2 = 2 µm, w = 0.4 µm, a = 7 µm. (b) A side view schematic of the metamaterials on a substrate: metamaterial crosses (gold, 100 nm thick), an Al_2O_3 dielectric spacer (t = 300 nm), another 200 nm layer of gold (the ground plane), and a silicon substrate. (c) Scanning electron microscope (SEM) image of the metamaterial array taken at a magnification of 4000 with unit cell outlined in white.

2.2 MMA Design

2.2.1 Geometric Characteristics

A schematic of the dual band metamaterial absorber in Fig. 2.1(a) and Fig. 2.1(b) shows the two different crosses, both gold, on a dielectric spacer made of Al_2O_3 arranged in a checkerboard pattern. The dielectric spacer resides on a second layer of gold acting as the ground

plane followed by a thick silicon substrate. The ERR cross structure allows for strong coupling to the incident electric field and minimal coupling to the incident magnetic field. The purpose of multilayered structure is to excite a magnetic response in resonance by driving antiparallel currents in the center of the cross and the portion of ground plane immediately behind it. This creates electric and magnetic responses that can be tuned separately: ε through the shape and size of the cross resonator and μ through the distance between the cross and the ground plane [31].

2.2.2 Simulation

Simulations of the dual band absorber are done using the finite difference frequency domain solver CST Microwave Studio [45]. Periodic boundary conditions simulate an infinite array and the incident light is modeled as a plane wave with a wavevector perpendicular to the array surface. The electric and magnetic components of the wave were parallel to the two arms of the cross structures; as the cross has four-fold rotational symmetry and the light comes in at normal incidence, the polarity of the wave is irrelevant. The gold was simulated as a Drude metal with conductivity derived from Eq. 1.24 [2]:

$$\sigma(\omega) = \varepsilon_0 \frac{\omega_p^2}{\omega_c - i\omega}, \tag{2.5}$$

with the plasma frequency $\omega_p = 2\pi \times 2175$ THz and collision frequency $\omega_c = 2\pi \times 6.5$ THz [69]. Optical constants for Al_2O_3, the dielectric spacer, were obtained through a frequency dependent model and input into the frequency domain solver with the data taken from a study done on Al_2O_3 films [70]. In the study, reflection and transmission measurements were taken over a wavelength range of 5 μm to 50 μm. Using this spectrophotometric data and Fresnel's equations, the dielectric function ($\varepsilon = \varepsilon_1 + i\varepsilon_2$) was obtained and is shown in Fig. 2.2(b) [70].

The results of the solver simulations are S-parameters collected at ports in front of and behind the structure. The absorption in terms of the S-parameters is:

$$A = 1 - R - T = 1 - |S_{11}|^2 - |S_{21}|^2 \tag{2.6}$$

where S_{11} is the reflection coefficient and S_{21} is the transmission coefficient. As stated, the ground plane thickness and loss prevents transmission ($S_{21} = 0$). Therefore, by minimizing the reflection, it is possible to create a near-unity absorber. By manipulating the geometry (size, thickness, distance between respective layers of the structure), we can optimize the structure to obtain high absorption. The simulated absorption is displayed on the red curve in Fig. 2.2(a).

To investigate the underlying absorption mechanism for the metamaterial and to understand the origin of the two absorption bands, we computationally monitored the magnetic field in the metamaterial multilayer structure. The simulated magnetic field distribution is shown in Fig. 2.3 where Fig. 2.3(a) and Fig. 2.3(b) display the magnetic field at the two impedance matched wavelengths. It is clear that the smaller sized cross resonates at 6.25 μm while the larger sized cross resonates at 8.45 μm. More importantly, both of the crosses seem to have little excitement outside of their respective wavelengths.

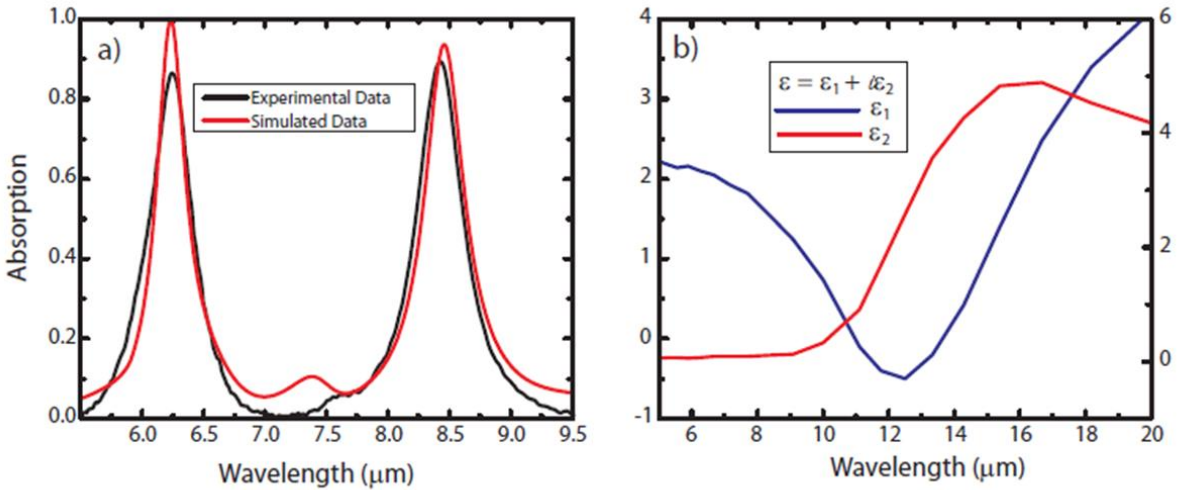

Fig. 2.2 – Experimental and Simulated Absorption (a) A graph showing the comparison of simulation to experiment. (b) Dielectric constants of Al_2O_3 taken from Eriksson (1981).

2.2.3 Fabrication

The absorber array fabrication starts with e-beam deposition of 200 nm of gold, the ground plane, on a thick silicon substrate (approximately 350 μm). This is followed by atomic layer deposition (ALD) of a 300 nm thick layer of Al_2O_3. E-beam lithography is then used to

pattern the absorber array design on a 140 µm x 140 µm area. This contains approximately 400 unit cells (4 cross absorbers per unit cell) hence approximately 1600 individual cross absorbers. Fig. 2.1(c) shows an SEM image of the fabricated sample.

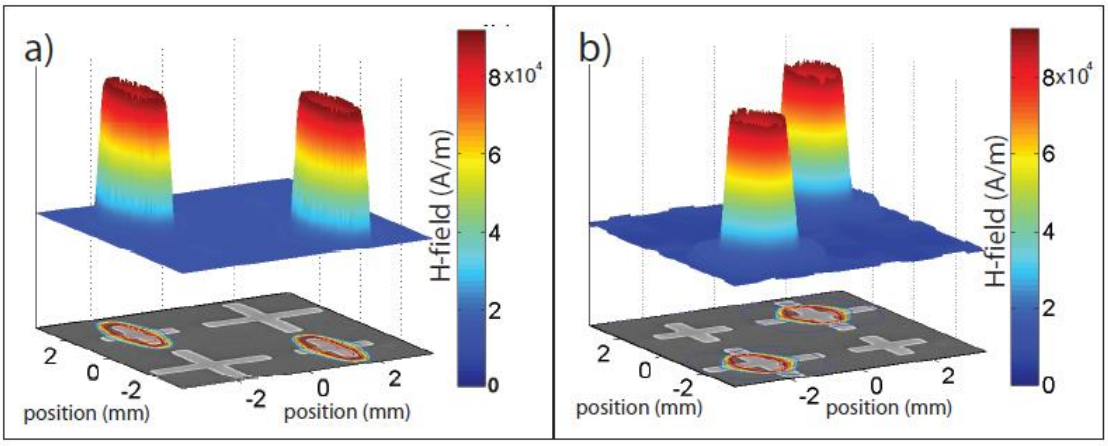

Fig. 2.3 – Simulated H-Field Concentration The magnitude of the H-field plotted on the surface of the dielectric spacer (just behind the gold crosses). Both a 3D plot and a contour map are shown. (a) The H-field plotted at 6.25 μm; the smaller cross is resonating. (b) The H-field plotted at 8.45 μm; the larger cross is resonating. The simulations are displayed on an SEM picture of the sample.

2.3 Results

2.3.1 Characterization Method

The characterization of our dual band metamaterial absorber is done using an IR microscope in tandem with a Fourier Transform Infrared (FTIR) spectrometer, allowing for the acquisition of both spectral and spatial information through a raster scan process. We utilize a KBr beam splitter in the spectrometer, which is calibrated for a wavelength range of 2.5 μm to 25 μm. The detector is a liquid nitrogen cooled MCT detector housed in the infrared microscope, suitable for the same wavelengths. Using a 15x objective we are able to optically view the array and set up the raster scan points to be measured, thus gaining spatial information about the sample.

2.3.2 Absorption Characteristics

Fig. 2.2(a) shows a comparison of simulated data and data from a single experimental measurement. Using the physical parameters laid out in Fig. 2.1 and the dielectric loss tangent and permittivity taken from the literature [70], the results of our experiment are very close to simulated data. We are able to achieve absorptions as high as 89 % for the experimental results; there are two clear bands of high absorption at 6.25 μm and 8.45 μm.

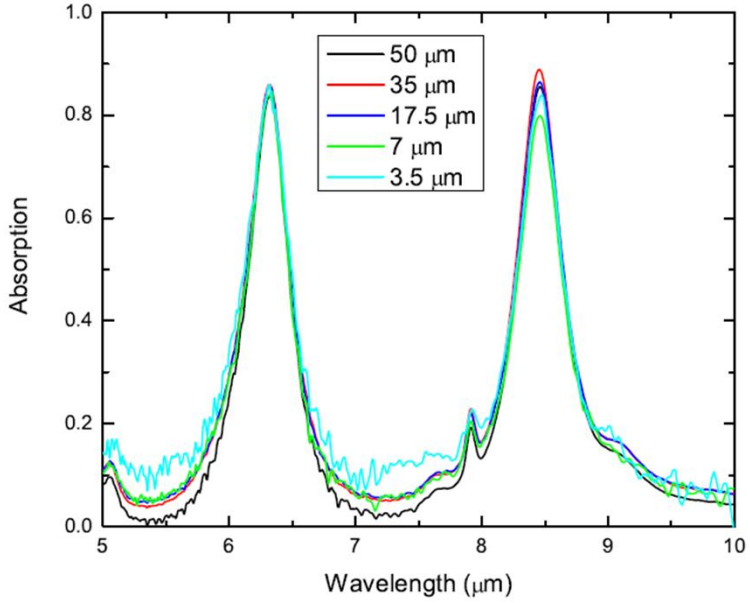

Fig. 2.4 – Experimental Absorption for Various Aperture Settings The absorption of the metamaterial array as a function of wavelength for various aperture settings. All aperture resonances (6.25 μm and 8.45 μm) agree. As the aperture size becomes smaller, the signal to noise ratio decreases.

2.3.3 Hyperspectral Imaging

Another goal of the dual absorber array is exploration of the spatial dependence of the electromagnetic response. The infrared microscope houses adjustable knife-edge apertures opaque to IR radiation. This allows us to also measure absorption as a function of aperture size as seen in Fig. 2.4, where we show hyperspectral data for a single spatial position located at the center of the array. The aperture has adjustable horizontal and vertical dimensions; we use a square aperture with sides of length 50 μm, 35 μm, 18 μm, 7 μm, and 3 μm. The 7 μm aperture size would hypothetically be imaging one unit cell at a time while the 3 μm aperture size would hypothetically be imaging a single cross absorber. It is clear from the measurements that al-

though the signal-to-noise ratio (SNR) decreases as we decrease the aperture, the amplitude and frequency of the absorption peaks remains fairly constant.

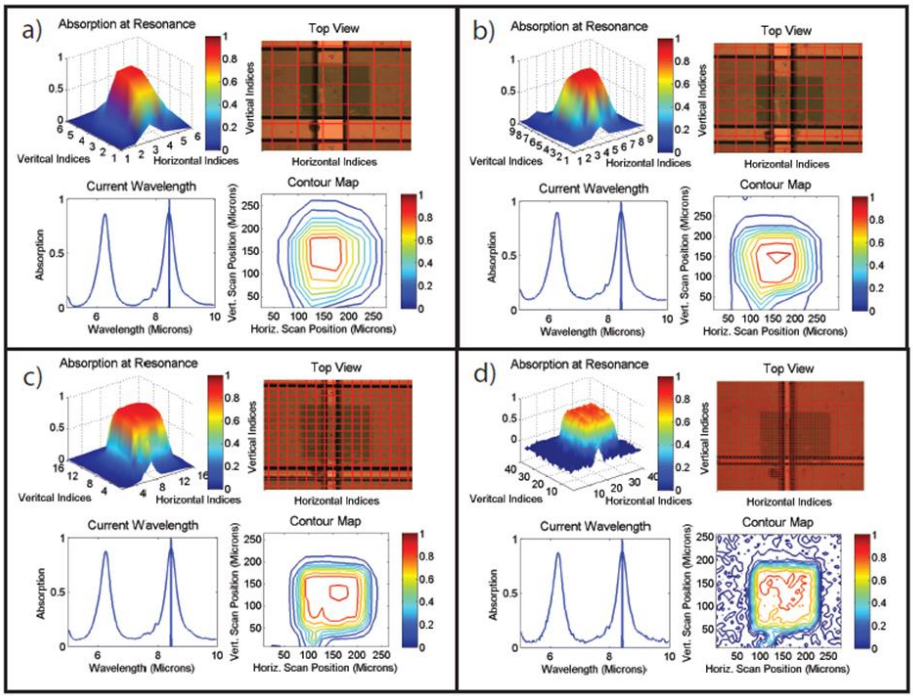

Fig. 2.5 – Spatially Dependent Absorption Multimedia file showing the spatial dependence of the absorption based on aperture size. All four animations show the absorption as a 2-dimensional spatial map while progressing through the incoming wavelength of light. (a) 50 μm aperture (Movie 2.5.1). (b) 35 μm aperture (Movie 2.5.2). (c) 18 μm aperture (Movie 2.5.3). (d) 7 μ aperture (Movie 2.5.4).

It was also of interest to investigate the effect that aperture size has on the imaging resolution. We test this by doing a series of measurements using the programmable XY stage to raster scan across a known area with a known aperture size to get spatial information from the sample. In the first demonstration of the spatial imaging resolution we take area measurements of the entire array surrounded by a gold ground plane for aperture sizes 50 μm, 35 μm, 18 μm, and 7 μm. The area measured is 280 μm x 280 μm. Our goal in doing this measurement is to characterize, based on aperture size, how resolved the array was compared to the background. We are able to create animations that scanned through wavelengths 5 μm to 10 μm, attached as Media 1 - Media 4, stills shown in Fig. 2.5, in order to best show the four dimensional data: absorption as a function of two spatial dimensions and one wavelength dimension. The upper left

panel shows the absorption as a function of spatial position in a 3D plot, in which the z axis and the colorbar denote the absorption at a single wavelength. The lower left panel shows the hyper-spectral absorption at a single spatial position with a marker showing the current wavelength of the animation. The upper right panel shows an optical image of the area being measured, with each grid point denoting the position of a spatial measurement. On each optical image the size of the knife-edged aperture for that animation is displayed (sides of length 50 μm, 35 μm, 18 μm, and 7μm). The lower right panel shows a top view of an absorption contour map as a function of spatial position, also displayed at the wavelength marked in the lower left panel. It is clear from the animations that, in spite of the noise in the measurement, the data taken with the 7 μm aperture resolves the array very clearly. Whereas the 50 μm aperture size has a rounded transition

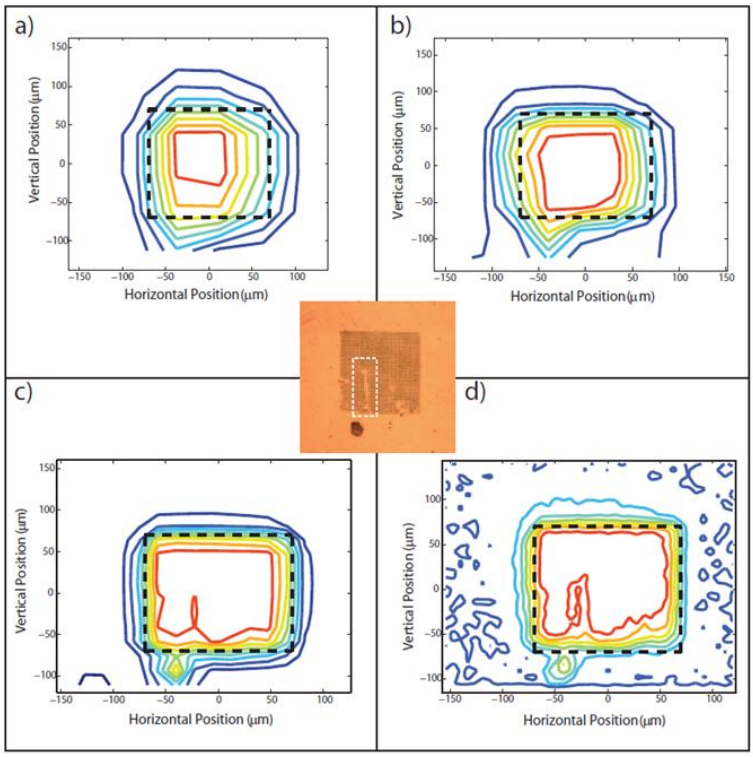

Fig. 2.6 – Absorption Contour Maps Absorption at resonance as a function of spatial position (shown in μm) is shown for each of the aperture settings. (a) 50 μm aperture, (b) 35 μm aperture, (c) 18 μm aperture, and (d) 7 μm aperture. The area scans were taken over a combination of the metamaterial array and the surrounding gold (as shown in the media files of Fig. 4). (e) Optical image of the metamaterial array and surrounding area. A blemish is circled that becomes apparent in the contour graphs (c) and (d). All contour graphs are shown at 8.45 μm resonance.

from the MM array to the gold background, the 7 μm aperture shows a sharp contrast between the two.

In Fig. 2.6 we show contour plots displaying the absorption as a function of the two spatial dimensions for four of the aperture sizes at a single wavelength (the resonance at 8.45 μm). The colorbars on the right of the figures show the scale at which the contour lines were drawn. Fig. 2.6(e) shows an optical image of the metamaterial array. It is clear that as the aperture size decreases, the IR image (the contour maps) is able to pick up more and more of the specific details of the array. For example, in the 50 μm and 35 μm aperture settings, the defect labeled with a red circle in Fig. 2.6(e) is not visible. However, for the 18 μm and 7 μm aperture settings, this defect becomes visible. An outline of the approximate position of the metamaterial array is shown in gray for each aperture size. Again, the superior resolution of the 7 μm aperture raster scan becomes more apparent in that it more clearly maps out the threshold between the MMA array and the surrounding ground plane. It captures the square shape of the metamaterial array in opposition to the 50 μm aperture in which the contours are rounded. As the aperture size decreases, less spatial averaging is done and the individual elements of the array become more apparent.

In another demonstration of the spatial dependence of the electromagnetic response of our structure we take various line scans across the array, i.e. we move the programmable XY stage across the x-axis to measure various spatial positions. For the four larger aperture sizes (50 μm, 35 μm, 18 μm, and 7 μm) each measurement images the same line, approximately 280 μm long, with the metamaterial array centered in the middle 140 μm with gold on either side. Depending on the aperture size, a different amount of spatial measurements are taken for each aperture size: 6 measurements for the 50 μm aperture setting, 8 measurements for the 35 μm aperture setting, 16 measurements for the 18 μm aperture setting, and 40 measurements for the 7 μm aperture setting. Each line scan is done so that the subsequent measurements did not overlap,

i.e. the step size was equal to the aperture size. The 3 µm aperture requires a long integration time in order to minimize noise so the line scan has less points than for the other aperture sizes; 15 measurements were taken, each 3 µm apart. Fig. 2.7(a) plots the absorption at a single frequency as a function of spatial position for all aperture settings. The data for the four larger aperture measurements are all shown at the 8.45 µm resonance while the data for the 3 µm aperture is shown for both resonances. The metamaterial array's edge is at the zero position on the x axis with gold in the negative region and the absorber array in the positive region. In Fig. 2.7 (b) we show the full measurements for the four larger apertures where the metamaterial array lies between x = -70 µm and x = 70 µm. The metamaterial boundary is represented by gray lines in Fig. 2.7(b). The goal of these measurements is to see how sharply the obtained absorptions transitioned from mirror to absorber. As shown in Fig. 2.7, the smaller the aperture size, the more sharply we see this transition. In the 7 µm aperture line scan (shown as the dark blue line), there are very few "transition points" and nearly all measurements are either show high reflection or high absorption. However, it can also be seen in Fig. 2.7(a) that for the 3 µm and 7 µm apertures the absorption as a function of position is not a true step function. This implies that the relationship of the surrounding absorbers, i.e. interelement coupling, is important.

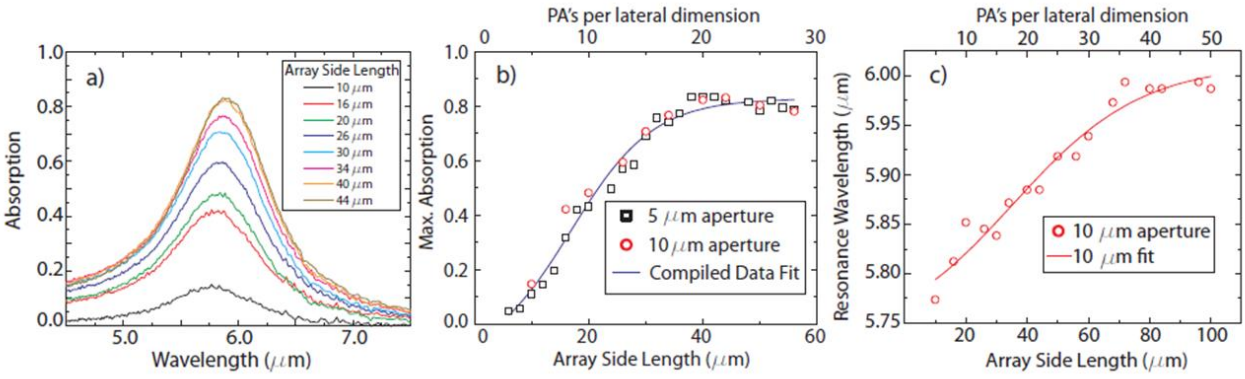

Fig. 2.7 – Array Truncation Effects (a) Direct results obtained for the variously sized arrays taken with an aperture size of 10 μm x 10 μm. (b) Compiled spectral data for maximum absorptions for various array sizes. Data was gathered for two aperture sizes to confirm the independence of absorption and aperture size. (c) The location of the maxima of each array as a function of the side length in microns. Both the array size and the number of MMA elements in the array are shown on the x axis in (b) and (c).

2.3.4 Array Truncation Effects

The effect of interelement coupling can be further investigated by varying the size of the metamaterial array. Measurements are done on multiple arrays with varying total lateral dimensions, each consisting of single resonance MMAs. The MMA used in these measurements has a strong absorption at $\lambda_0 = 6$ μm and has a unit cell size of 2 μm. In order to test nearest neighbor interaction, measurements are taken with a constant aperture size at the center of each of the differently finite sized arrays. The obtained spectra can be seen in Fig. 2.8(a). Results are shown for arrays ranging from 5 x 5 MMAs to 22 x 22 MMAs and were obtained with an aperture size of 10 μm. Fig. 2.8(b) displays the maximum absorption measured (at resonance) as a function of array side length. This is shown for the 10 μm aperture (taken from the data shown in Fig. 2.8(a)) and also a 5 μm aperture. Although we were able to image smaller arrays with the 5 μm aperture, there is an inherent level of noise associated with an aperture this small and therefore the results from the 5 μm aperture are not displayed in Fig. 2.8(a). It should be noted, however, that the 5 μm aperture results confirm the results obtained for the 10 μm aperture. A plot of the resonance wavelength as a function of array side length is shown in Fig. 2.8(c).

2.4 Discussion

Metamaterials, often described as "photonic atoms", are governed by Maxwell's equations. Their subwavelength nature allows them to be characterized as an effective medium and have effective optical constants. With the use of spatial microscopy, we can begin to fully describe the nature of the behaviors of these optical properties.

Using the knife edged aperture, we were able to see in Fig. 2.4 a comparison of the spectra for each aperture size. It is clear that we obtain similar data for all aperture sizes, both in the magnitude of the absorption and the wavelengths at which the absorption peaks were measured. One may think that this suggests the crosses act individually rather than coupling strongly. For example, when we image with the 7 μm aperture size, we would hypothetically be imaging one unit cell, yet we are obtaining the same absorption characteristics as if we measured

a 50 μm x 50 μm area. It brings up the question of whether the presence of a surrounding array of identical structures affects the performance of a single unit cell. If the individual absorbers are acting alone and the absorption does not depend on the aperture size, the effective optical constants of our sample, μ and ε, should also not depend on aperture size as $A = A(\mu, \varepsilon)$. Is it false to refer to our metamaterial absorber array as an effective medium because the optical constants are not effective at all but dependent on each unit cell?

The reason that we can, indeed, consider the dual absorber array as an effective medium is that the crosses do not act individually, as postulated above. Even though we are irradiating only a small portion of the sample with light, we are seeing an effective response. This is due to the fact that the individual crosses exhibit neighbor interactions that spread beyond the small portion being illuminated. Our array size can be considered effectively infinite as it is much larger than both the unit cell and the resonant wavelengths of the sample; the array is 2.8 mm x 2.8 mm, i.e. 1600 total unit cells while our resonant wavelengths are 6.25 μm and 8.45 μm. This gives an absorption that is independent of aperture size and similar to the simulated spectrum as our medium holds effective and spatially uniform optical constants in spite of the aperture size used.

This can also be seen in the 3 μm aperture measurements. Hypothetically we should be imaging a single cross at a time; there are four crosses per unit cell, two that resonate at 6.25 μm and two that resonate at 8.45 μm. This suggests that if the absorbers are truly independent of one another, we should measure an overwhelmingly stronger peak for either the 6.25 μm resonance or the 8.45 μm resonance when using the 3 μm aperture, depending on the specific absorber we were imaging. The fact that we see two strong resonances when imaging with the 3 μm aperture size suggests that there is interaction between neighboring absorbers, causing them both to resonate.

If our sample is exhibiting interelement coupling, then our absorption should depend on the size of the array, as investigated in Fig. 2.8. Even though the same area is irradiated, i.e. even though the 5 x 5 array and the 22 x 22 array have the same size area imaged, the truncated arrays

should lower absorption due to the lack of interelement coupling. This is because the lack of nearest neighbors for the smaller arrays lessens the overall effective medium phenomenon.

We see that this is the case in Fig. 2.8(a). However, we also see that the absorption seems to saturate at a certain array size. This can be seen even more clearly in Fig. 2.8(b) in which the maximum absorption increases as a function of array side length and then flattens out at an approximate lateral dimension of 20 MMAs. This can be interpreted as the point at which the absorber array becomes "infinite" and the sample can truly be treated as an effective medium. This is the same phenomenon witnessed in the dual absorber array measurements (specifically Fig. 2.4). Our array contains 1600 unit cells, far greater than the 400 unit cells in the array mentioned above, is essentially infinite, and therefore has effective optical constants that do not vary spatially.

The fact that the resonant frequency shifts (Fig. 2.8(c)) implies that the effective optical constants are dependent on the array side length. The shift in the absorption resonance tells us that the impedance is matched at a different spectral location, which means that one or both of the optical constants was altered according to Eq. 2.2. However, as the array size grows and the outer absorbers become more distant from the excitation and less interactive, we would predict that this shift diminishes. This is confirmed in Fig. 2.8(c) where we see that the graph levels off once the array size reaches approximately 36 x 36 MMAs.

Interelement coupling has been studied extensively in metamaterials. Perhaps some of the most relevant theoretical [71, 72] and experimental [73] work concerns magnetoinductive (MI) waves. MI waves are the phenomenon in which elements that are not directly excited with electromagnetic waves can still become resonant via inductive coupling with their neighbors. Not only has it been shown that constituent elements couple, but that their relative spacing and other lattice parameters can greatly influence the effective values of ε and μ, and therefore other optical parameters such as absorption, reflection, and transmission. Both theoretical [74] and experimental [75 – 77] work has been done concerning the tuning of metamaterial resonances via

lattice parameters. These studies support our postulate that we are seeing interelement coupling and that changing such lattice parameters as the outer dimension will change the amplitude and wavelength of the measured absorption.

With better understanding of MMAs, we can begin to more effectively utilize them in application. Metamaterial absorbers have drawn attention for their proposed usefulness in single pixel imaging. As we will discuss in chapters 5 and 7, MM spatial light modulators (SLM's) can be used to encode light and greatly increase the signal-to-noise ratio when imaging [78]. In addition, they can often penetrate parts of the electromagnetic spectrum that are difficult to image in, such as the THz regime [78, 79]. As the SLM imaging pixels are finite in size and may be only slightly larger than the wave-length of light, it is important to know how they absorb radiation in order to optimize the SLM design.

In this study we have designed, simulated and experimentally demonstrated a dual band meta-material absorber with absorption up to 89 % at two resonances: 6.25 μm and 8.45 μm. By raster scanning our sample we are able to gain both spectral and spatial information. One important concept we can gain from these measurements is the sharp resolution we were able to obtain by reducing the aperture size. We also explore the idea of interelement coupling and the absorber array as an effective medium. With this analysis, it is possible to gain more detailed information about the nature of metamaterials. By looking closely at the spatial dependence of these structures, specifically in terms of their nearest-neighbor interaction and their group versus individual resonant behavior, we can begin to determine the full spatial and spectral dependence of metamaterial absorbers.

3. Imaging Theory

3.1 Long Wavelength Imaging

3.1.1 Imaging in the THz Gap

Terahertz radiation has great potential for imaging applications [80, 81] due to its ability to penetrate most dielectric materials and non-polar liquids. Its harmless interaction with human tissue suggests imaging in this regime has immediate applicability in the fields of biodetection [82], system inspection [83], and detection of illegal drugs [84]. However, a significant limitation currently preventing wide-spread THz imaging is the absence of efficient sources and detectors operating in the "THz gap" [33].

3.1.2 Current Techniques for Imaging

Although there exists a great technical difficulty in feasibly performing THz imaging, there has been moderate progress over the past 25 years. Multi-element detector schemes, both microbolometer arrays [85, 86] and electro-optic sampling with high-performance CCD cameras [87], provide accurate and real-time THz images. However, these imaging systems often require high powered sources and/or expensive complex detectors that lack the sensitivity of single element detectors. The use of a single detector has been employed to obtain THz images by mechanically raster scanning the object plane to acquire spatial information [88]. While the latter technique has the benefit of high spatial resolution and accurate imaging, major shortcomings are the long acquisition time [89] and the mechanical nature of the scanning system.

However, a different approach utilizing a single sensor may be implemented, where the radiation is spatially modulated at the image plane through a coded aperture before being directed to a detector. The idea of a single pixel camera dates back as early as 1949 when Golay suggested its use [90]. However, single pixel imaging did not begin in earnest until the development of the modern computer and was first demonstrated in 1976 as an infrared hyperspectral imager [91].

Although there has been some progress in the optical using digital micromirror devices [92] and in the infrared, THz, and mm-Wave using static [93, 94] or low resolution masks [95, 96] there has yet to emerge a viable solution feasible for real-world applications.

3.1.3 Metamaterials Enable Efficient SLM Devices

In the following chapters, I will show that metamaterials have provided a means to create efficient and capable SLMs in the THz regime. This has allowed for the possibility of creation of a single pixel imaging system in the THz regime that is all electronic and has no moving parts. The use of MMs in single pixel imaging will be discussed further in chapters 4 – 7.

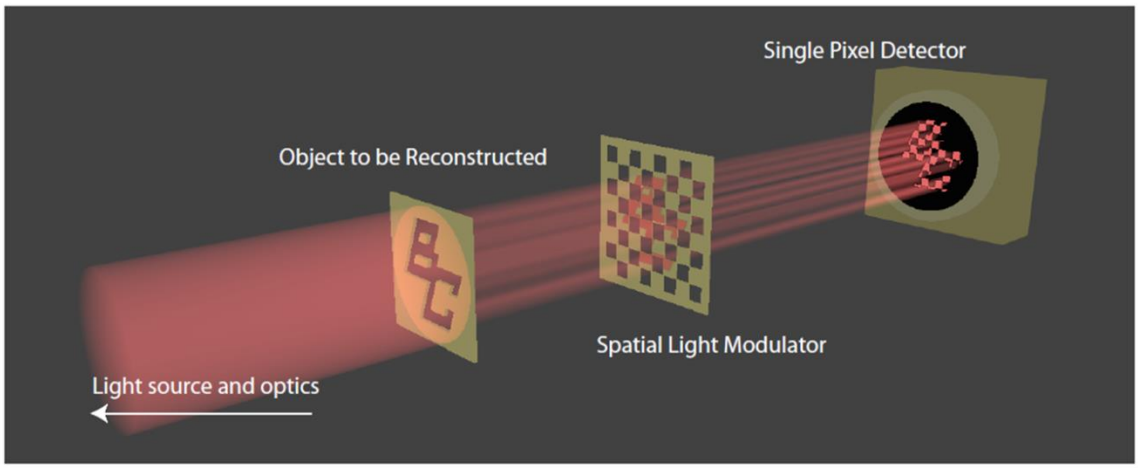

Fig. 3.1 – Conceptual schematic of single pixel imaging system.

3.2 Single Pixel Cameras

3.2.1 Introduction to Single Pixel Imaging

Single pixel camera architectures generally use one intensity based detector to acquire spatial information. The problems associated with the THz regime mentioned in Section 3.1 make the creation of detector arrays difficult and expensive, meaning these imaging systems are very useful at longer wavelengths. Typical systems use optics to image an illuminated object onto the spatial light modulator, which selectively blocks a spatial subset of the image; the passed radiation is then sent to the detector. By doing this with many different patterns or 'masks,'

enough information can be gathered to reconstruct the image incident on the SLM. A conceptual schematic is shown in Fig. 3.1.

3.2.2 Single Pixel Imaging Mathematical Theory

We can consider an *N*-element image *X*; single pixel measurements taken after the spatial modulation from the SLM can be represented as an *M*-element vector *Y*. Each measurement, y_i, is a vector multiplication of the image and the particular mask on the SLM at that time:

$$y_i = \sum_{j=1}^{N} \Phi_{ij} x_j \tag{3.1}$$

or the matrix equation $Y = \Phi X$. The above matrix equation represents the image *X* as being expanded in some basis (represented by Φ). *X* can be recovered for well-defined matrices Φ through an inverse matrix equation: $X = \Phi^{-1} Y$ [97]. Utilizing different types of masks one can obtain *M* measurements as a time sequence from the single pixel detector. There are many different bases that the image can be expanded in for sampling, i.e. different types of masks displayed sequentially on the SLM. For example, some common bases are: raster-scan style masks (i.e. where Φ is the $N \times N$ identity matrix), Hadamard matrices (to be explained below), and random matrices.

Although there are many benefits to using a single pixel detector, it should be noted that it often increases image acquisition time over THz cameras utilizing focal plane arrays due to the fact that measurements must be taken serially, rather than in parallel. However, using the multiplexing technique along with compressed sensing (discussed below), allows for faster image acquisition than a raster-scan technique due to the fact that the image can be reconstructed with less measurements than pixels resolved. Additionally, the allowed decrease in source power over FPA implementations outweighs the fact that acquisition time is somewhat increased when moving towards a real-world device.

Fig. 3.2 shows a general schematic of a single pixel imaging apparatus. This includes several key components which are part of all single pixel imaging systems: (a) the source, (b) the object being imaged (X), (c) imaging optics that create a conjugate image plane on the SLM, (d) the SLM, which displays encoding masks (Φ), (e) focusing optics, and finally (f) the single pixel detector, which collects a single measurement for each mask (Y). While the specifics of source, optics, detector, and SLM might change, they each represent the same component in the theory of single pixel imaging and will be consistent throughout the rest of the chapters.

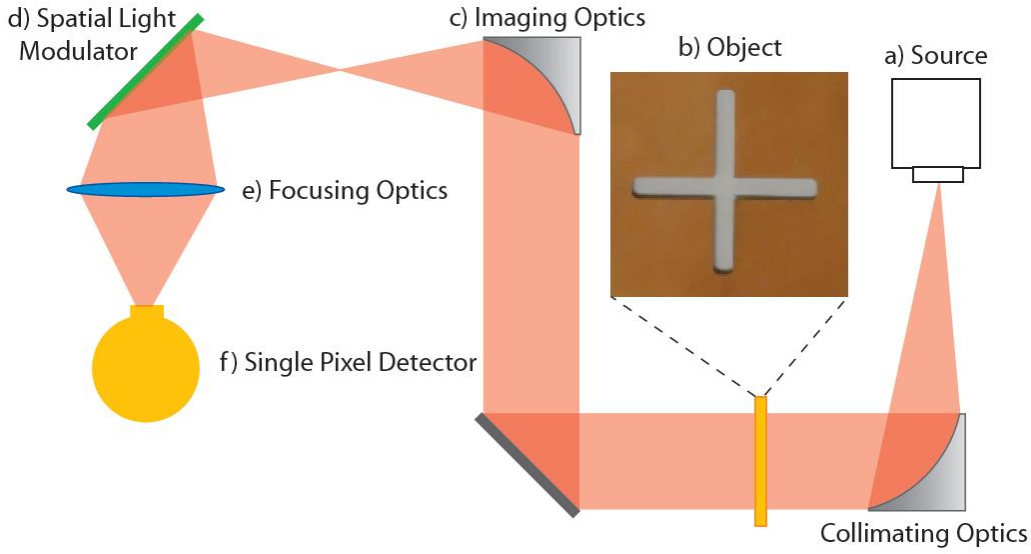

Fig. 3.2 – Single Pixel Imaging Apparatus General apparatus for single pixel imaging system, which will apply to all further chapters. Key components: (a) the source, (b) the object being imaged (***X***), (c) imaging optics that create a conjugate image plane on the SLM, (d) the SLM, which displays encoding masks (**Φ**), (e) focusing optics, and finally (f) the single pixel detector, which collects a single measurement for each mask (***Y***).

3.2.2 Types of Measurement Matrices

Raster-scan style masks stem from the well-known raster-scan technique in which the spatial pixels are measured serially. This results in a measurement matrix equal to the $N \times N$ identity matrix. Random matrices can also be used in which each mask has a random distribution of [1, 0], [1, 0, -1], or [1, -1] values.

Additionally, masks can be derived from Hadamard matrices. Hadamard matrices are square matrices comprised of [1, -1] values in which each row is orthogonal to all other rows [97]. Hadamard matrices are particularly useful in that they have an analytical inverse, easing

image reconstruction. For a Hadamard matrix of order N (i.e. an $N \times N$ matrix), the inverse can be expressed as $H_N^{-1} = \frac{1}{N} H_N^T$ where H_N^T is the transpose of the N^{th} order Hadamard matrix [97]. Several examples of Hadamard matrices are shown in Fig. 3.3.

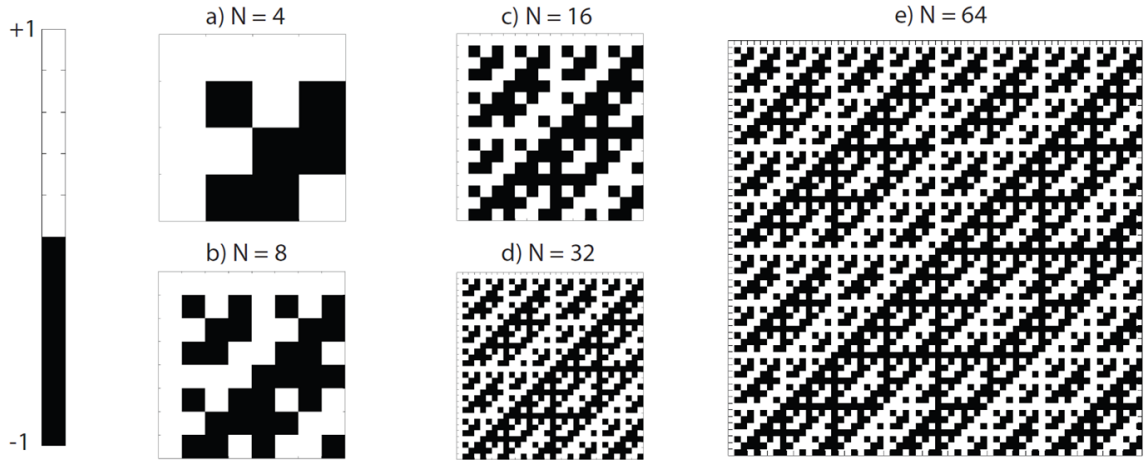

Fig. 3.3 – Hadamard Matrices Example Hadamard matrices for several dimensions. A Hadamard matrix of order $n_1 \times n_2 = N$ would constitute N $n_1 \times n_2$ consecutive, orthogonal masks on the SLM. Matrices shown are (a) 4 × 4, (b) 8 × 8, (c) 16 × 16, (d) 32 × 32, and (e) 64 × 64.

Deriving masks from Hadamard matrices can increase signal to noise in the reconstructed image over a standard raster-scan technique (i.e. in which $\Phi = I_N$) and results in low mean square error (MSE) [97]. Let Y represent the vector of N measurements taken in a system with a measurement matrix Φ and an image X:

$$Y = \Phi X + e, \tag{3.2}$$

where e represents an N-element vector of error associated with each measurement. For $e = 0$ we can reconstruct the image exactly:

$$X = \Phi^{-1} Y. \tag{3.3}$$

However, for real systems, we can reconstruct an estimate at best: $\hat{X}$. We assume that each element of *e* is random and independent of the intensity of the signal, that the average value of all elements in *e* is 0 (i.e. $E\{e_j\} = 0$) with a variance of σ^2, and that the errors in the different measurements are independent such that $E\{e_i e_j\} = 0$ for $(i \neq j)$. We assume that our estimate will be some linear function of the measurements: $\hat{X} = \Theta Y$ for some $N \times N$ matrix Θ. The assumption that our estimate is unbiased (i.e. $E\{\hat{X}\} = X$) suggests that $\Theta = \Phi^{-1}$. To choose the best measurement matrix Φ we attempt to minimize the average MSE. We define the MSE for a reconstructed pixel as: $\varepsilon_j = E\left\{\left(\hat{x}_j - x_j\right)^2\right\}$ with the average being $\varepsilon_{\text{avg}} = \frac{1}{N}\sum_{j=1}^{N} \varepsilon_j$. Based on the fact that $\hat{X} = \Phi^{-1}Y = X + \Phi^{-1}e$ we determine the error to be $\hat{X} - X = \Phi^{-1}e$. For an individual reconstructed pixel, the error is $\hat{x}_j - x_j = \sum_{i=1}^{N} \phi_{ji}^{-1} e_i$ with the MSE represented as: $\varepsilon_j = E\left\{\left(\hat{x}_j - x_j\right)^2\right\} = \sigma^2 \sum_{i=1}^{N}\left(\phi_{ij}^{-1}\right)^2$. The average MSE across all pixels is then

$$\varepsilon_{\text{avg}} = \frac{1}{N}\sum_{j=1}^{N} \varepsilon_j = \frac{1}{N}\sigma^2 \sum_{j=1}^{N}\sum_{i=1}^{N}\left(\phi_{ij}^{-1}\right)^2 = \frac{1}{N}\sigma^2 \text{Trace}(\Phi^{-1}(\Phi^{-1})^T) = \frac{1}{N}\sigma^2 \text{Trace}((\Phi^T\Phi)^{-1}) . \quad (3.4)$$

To minimize the MSE we attempt to find a measurement matrix Φ that minimizes $\text{Trace}((\Phi^T\Phi)^{-1})$.

In 1944 Hotelling proved that the lowest MSE by a measurement matrix Φ in a weighing design (i.e. $\phi_{ij} = \pm 1$) is $\varepsilon_j \geq \frac{\sigma^2}{N}$ with the equality only being reached if Φ is a Hadamard matrix [97]. We start with the inner product of the j[th] row and column of Φ^{-1} and Φ respectively: $\phi_{j1}^{-1}\phi_{1j} + \cdots + \phi_{jN}^{-1}\phi_{Nj} = 1$ as the product of Φ and Φ^{-1} is the identity matrix. By the Cauchy-Schwarz inequality:

$$\left(\phi_{j1}^{-1}\phi_{1j} + \cdots + \phi_{jN}^{-1}\phi_{Nj}\right)^2 \leq \left(\left(\phi_{j1}^{-1}\right)^2 + \cdots + \left(\phi_{jN}^{-1}\right)^2\right)\left(\phi_{j1}^2 + \cdots + \phi_{jN}^2\right)$$

$$1 \leq N\left(\left(\phi_{j1}^{-1}\right)^2 + \cdots + \left(\phi_{jN}^{-1}\right)^2\right) \tag{3.5}$$

as each element of the measurement matrix is restrained between [1, -1]: $|\phi_{ij}| \leq 1$. Therefore,

$$\frac{\varepsilon_j}{\sigma^2} = \sum_{i=1}^{N}\left(\phi_{ij}^{-1}\right)^2 \geq \frac{1}{N} \text{ and } \varepsilon_j \geq \frac{\sigma^2}{N}. \tag{3.6}$$

For this to be an equality, the j[th] row and column of Φ^{-1} and Φ respectively must be parallel vectors: $\left(\phi_{j1}^{-1} + \cdots + \phi_{jN}^{-1}\right) = c_j\left(\phi_{1j} + \cdots + \phi_{Nj}\right)$. Substituting these relationships into the above equation we find that $c_j = \frac{1}{N}$ and $\Phi^{-1} = \frac{1}{N}\Phi^T$ or

$$\Phi\Phi^T = NI_N, \phi_{ij} = \pm 1. \tag{3.7}$$

Therefore, for the above MSE equation to be an equality and for the MSE to be the lowest value possible, $\Phi = H_N$ i.e. the $N \times N$ Hadamard matrix.

We can also calculate the advantage in terms of signal to noise ratio (SNR). The root mean square SNR of the j[th] reconstructed pixel is $\text{SNR}_j^{\text{RMS}} = \sqrt{\frac{x_{\text{avg}}}{\varepsilon_j}}$. We can compare two cases: one in which we use the Hadamard matrix as the measurement matrix and the 'raster-scan' style measurement when $\Phi = I_N$.

$$\frac{\text{SNR}_{\text{rast.}}^{\text{RMS}}}{\text{SNR}_{\text{Had.}}^{\text{RMS}}} = \sqrt{\frac{\sum_{j=1}^{N}\varepsilon_{j,\text{Had.}}}{\sum_{j=1}^{N}\varepsilon_{j,\text{rast.}}}} = \sqrt{\frac{\sigma^2}{N\sigma^2}} = \frac{1}{\sqrt{N}}. \tag{3.8}$$

Hence by using Hadamard matrices we improve the SNR of our reconstruction by $\sqrt{N}$.

In addition, the Walsh transform can be used to multiplex and reconstruct the data. The main difference between the Walsh transform and the Hadamard transform is the order in which the masks are arranged in the measurement matrix Φ; however, the masks themselves are

identical. Rows of the Hadamard matrix are made of series +1's and -1's; each row can be thought of as a step-like function on the interval $-½ \leq t \leq ½$ where the values in that row of the Hadamard matrix determine the values for that function [97]. For the $N \times N$ Hadamard matrix, each row will cross the t-axis a different number of times ranging from 0 (i.e. all +1) to $N - 1$ (i.e. alternating +1 and -1 the entire row) [97]. The number of zero-crossings per row is termed the 'sequency.' The Walsh matrix is constructed by arranging the rows of the Hadamard matrix in order of increasing sequency [97, 98]. Walsh transforms have been used since the 1960's and were first utilized in the field of telecommunication engineering [98]. The Walsh transform has been used extensively for the compression of data with the majority of their information in lower sequencies [99].

3.3 Compressive Sensing

The well established Shannon sampling theorem states that a signal can be reconstructed perfectly if it is sampled above the Nyquist limit, or greater than twice it's maximum frequency: $f_N = 2f_{max}$ [100]. However, there is a mathematical theory known as compressive sensing stating that signals can be sampled at far lower frequencies than traditional methods [101]. This relies on two pieces of prior knowledge about the system: first, that the signal is sparse in some basis, second, that the signal be sampled incoherently [101].

It is well known that images can often be expanded in another basis to achieve sparsity, i.e. where the number of nonzero coefficients is less than the total number of coefficients. For example, a signal X with N elements is considered K-sparse if, when expanded in some alternate basis Ψ, it has K nonzero coefficients with $K < N$:

$$x_j = \sum_{i=1}^{N} \psi_{ij} s_i \text{ i.e. } X = \Psi S \text{ [92].} \tag{3.9}$$

This property is utilized in the well-known JPEG and JPEG2000 compression schemes [102], which consist of taking the full N measurements and discarding the $(N - K)$ negligible coefficients for compression. However, it has been shown that with knowledge of the image sparsity, a signal can be *sampled* compressively so that only $M < N$ measurements are made [103, 104]. This involves utilizing some $M \times N$ measurement matrix Φ:

$$Y = \Phi X = \Phi \Psi S = \Theta S \text{ [92]} \tag{3.10}$$

where, as stated above, each row of the matrix Φ represents a separate measurement (i.e. a separate mask shown on the SLM).

The problem then becomes how to sample the image intelligently and fulfil the property of incoherence. A property known as the restricted isometry property (RIP) will ensure that the signal can be reconstructed from less than the full set of samples [105, 106] when the measurement matrix satisfies certain conditions. With the $M < N$ samples, there are infinitely many vectors X' that satisfy the reconstruction requirement $\Phi X' = Y$ [92]. Yet, there are many methods to reconstruct the image with high accuracy, such as basis pursiut methods, greedy pursuit methods, as well as stochasitc and variational methods [92]. There are many compressive sensing reconstuction programs freely availble for use, including: FISTA [107], SpaRSA [108], and l_1-Magic [109].

4. Dynamic THz SLM via Photodoped Semiconductor

4.1 Introduction

THz transmission through semiconductors can be tuned through use of an optical pump beam. The basic idea involves using an optical beam with energy near the bandgap energy, exciting carriers, and changing the transmissive properties for THz.

In chapter 3 we detailed a theory of single pixel imaging. In the following chapter we describe an implementation of this design in the THz frequency regime using a spatially patterned optical beam to photodope a ρ –Si wafer to create a dynamic, reconfigurable THz SLM. Many of the THz components (such as the source and detector) were also used for the experimental setups in chapters 5 and 7.

4.2 THz Modulation via Photo-excitation

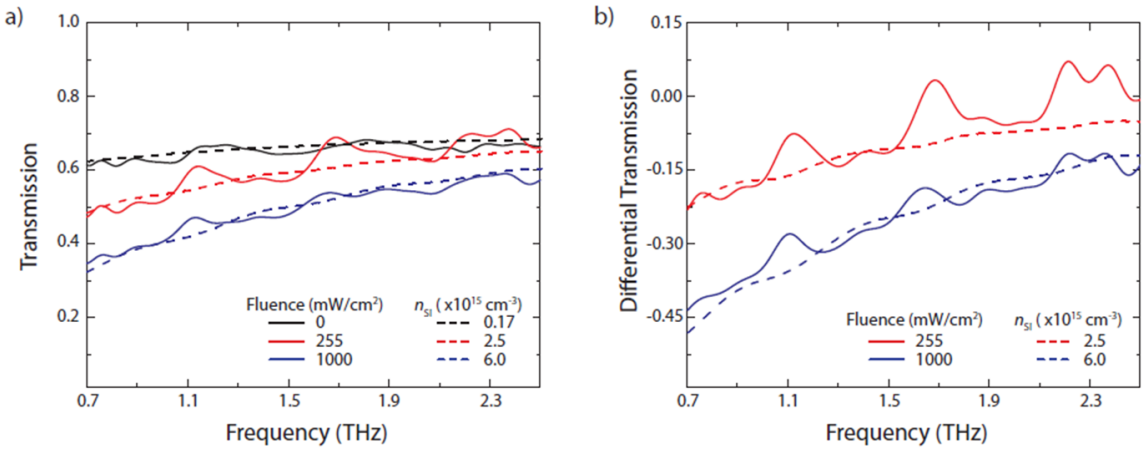

Fig. 4.1 - THz Modulation via Photodoped Silicon (a) Solid curves show the transmission of THz radiation through ρ -Si wafer as a function of frequency for several different optical fluence values. Measurements were done in atmosphere in FTIR system. The dashed curves show the simulated fits for increasing carrier concentration n_{Si} within the penetration depth (85 μm) of ρ -Si. (b) Dependence of the differential transmission on the optical fluence as defined in the text.

The photoexcitation of free carriers in semiconductors is a well understood process for both CW and ultrafast optical beams [110]. For ρ -Si substrates a higher carrier density can be generated by CW pump beams, compared to pulsed sources of identical average power, due to the relatively long carrier lifetimes in Si [111]. The change in the complex dielectric constant can be described by the Drude model (Eq. 1.24) [111 – 114].

$$\varepsilon_r(\omega) = \varepsilon_\infty - \frac{\omega_p^2}{\omega^2 + i\gamma\omega} \tag{4.1}$$

where we have included the term ε_∞ to account for high-frequency behavior due to the contributions of bound electrons: $\varepsilon_\infty = 11.7$. Other parameters include $= {}^{1}/_{\tau_c}$, the damping rate (with τ_c = 160 fs the average collision time [111, 114]), ω_p is the plasma frequency defined as $\omega_p^2 = {}^{n_{Si}e^2}/_{\varepsilon_0 m^*}$ with e the electron charge, ε_0 the free-space permittivity, and $m^* = 0.26m_e$ effective mass [114]. If we neglect the carrier diffusion and consider only free carrier generation and linear recombination in the semiconductor, the carrier density n_{Si} is proportional to the optical power of the pump beam and is modulated through photodoping [113]

$$n_{Si} = \frac{I_0(1-R)\tau}{2Ad\hbar\omega}, \tag{4.2}$$

where I_0 is average power, R is the reflectivity of Si at the pump wavelength, $\hbar\omega$ is the photon energy, τ = 25 μs is the carrier lifetime [115], A is the area of the laser excitation, and d is the penetration depth. At THz frequencies the photodoped charges correspond to a large increase in the absorption coefficient as a function of I_0, allowing for strong attenuation of incident THz electromagnetic waves.

We measured the THz transmission, shown as the solid curves in Fig. 4.1, through a 520 μm thick ρ-Si substrate (ρ > 10,000 ohm-cm) for increasing optical power using a 980 nm CW laser diode. We characterize the THz transmission using a Fourier Transform Infrared (FTIR) spectrometer, a mercury (Hg) arc lamp source, multi-layer Mylar beamsplitter, and liquid-helium cooled silicon bolometer. The size of the THz and optical beams was 4 mm and 9 mm,

respectively, at the plane where we placed the ρ-Si substrate. Etalons due to multiple reflections within the ρ-Si substrate were removed and the modified interferogram was Fourier transformed to obtain the sample spectrum. A similar procedure was performed for a reference with an open channel; division of the sample and reference spectra resulted in the frequency dependent absolute value transmission $T(\omega)$ and corresponding differential transmission $\Delta T = \left[T_p(\omega) - T_{p=0}(\omega)\right]/T_{p=0}(\omega)$ shown in Figs. 4.1(a) and 4.1(b), respectively. We observe broad-band attenuation of the THz signal where, at our maximum fluence of p = 1 W/cm^2, we measure a modulation depth of 43% at 0.7 THz. The undoped ($T_{p=0}(\omega)$, black curve) of Fig. 4.1(a) was performed in vacuum; however, due to technical limitations, transmission measurements for both photodoped cases were performed in air - leading to a reduced signal-to-noise which accounts for the large fluctuations in $T(\omega)$.

The dashed curves in Fig. 4.1 are the results of full wave 3D electromagnetic simulations where we model the resulting change in the transmission as a function of an increase in the ρ-Si conductivity using the commercial finite difference time domain (FDTD) solver CST Microwave Studio 2012. In simulation we define the ρ-Si within the penetration depth, d = 85 μm [111], as a Drude layer, described by Eqs. 4.1 and 4.2, with increasing n_{Si}. Below the penetration depth the ρ-Si is treated as a dielectric with a constant complex permittivity $\varepsilon_{Si} = 11.7 + 0.01i$. The photogenerated carrier density approached 6×10^{15} cm^{-3} for the maximum fluence, in agreement with previous work [111]. The strong frequency dependence of the imaginary component of the dielectric permittivity within the photoexcited region results in high absorption at lower frequencies and minor attenuation above several THz. The qualitative agreement between the model and experimental measurements demonstrate that optically controlled broadband THz modulation is possible. Since the carrier lifetime in ρ-Si of τ = 25 μs is the only fundamental limit to this technique, switching speeds beyond 10 kHz is achievable.

4.3 Experimental Setup

4.3.1 Imaging Apparatus

A schematic of the THz imaging system is presented in Fig. 4.2(a) and consists of both an optical beam path (red lines) and a THz beam path (gray lines). Note that the THz optical system has the key components pointed out in Fig. 3.2, i.e. the THz source, an object, imaging optics (here and off-axis parabolic mirror), a single pixel detector (here a bolometer), and a dynamic SLM. Here the SLM is a ρ –Si wafer modulated by a spatially patterned optical light (red path). The THz source is an Hg-Arc lamp which emulates a 5500 K blackbody. The source is used in conjunction with a long-pass filter (LPF-065 from Lakeshore) that blocks wavelengths shorter than 65 μ m (> 4.6 THz). The THz imaging optics consist of two 50.8 mm diameter 90° off-axis parabolic mirrors (OAPMs) each with an effective focal length of f_L =190.6 mm. The first OAPM is f_L from the source and back-illuminates the object a distance 150 mm away. The second OAPM, a distance 933 mm from the object, focuses the radiation and forms a conjugate image on the SLM 215 mm away. The system has an overall magnification of 0.23, mapping the 43.5 mm diameter object to approximately 10 mm at the SLM. An image was formed by placing a back illuminated patterned metal aperture between the OAPMs so that a THz image (10 mm in diameter) was formed at the SLM plane. The THz image is transmitted through the ρ-Si and focused using a 50.8 mm diameter TPX lens with f = 100 mm to the detector - a liquid-helium cooled silicon bolometer. The entire apparatus is enclosed and is purged by dry air at room temperature to reduce the THz absorption due to water vapor.

As stated, the dynamic THz SLM is achieved through photoexcitation of a ρ –Si wafer with an optical photodiode. Detection of the THz signal is performed with a lock-in detection technique. The laser diode power is modulated with a square wave at a frequency of 300 Hz, which in turn modulates the THz power detected. Output voltage from the Si-bolometer is input into a lock-in amplifier which provides the measured THz signal in Volts. Figures 4.2(c), 4.2 (d) show the measured lock-in voltage as a function of time for several successive masks; the

corresponding binary bitmap displayed on the DMD are shown above the raw data in Fig. 4.2 (d). The stabilization of the lock-in signal after switching between masks is close to 5 ms, with a SNR recorded for each measurement greater than 100; this is sufficient to allow us to acquire a THz measurement at the limits of the switching time of the DMD. We may estimate the total power of THz radiation used in our imaging apparatus since our bolometer has a calibrated responsivity of 2.64×10^5 V/W at 300 Hz. Our DMD may be configured to modulate all pixels on and off, from which we measure a lock-in signal of 130 mV. Thus our THz image consists of a maximum modulated THz power of 96 nW over an integrated bandwidth from 0.2 - 4.6 THz.

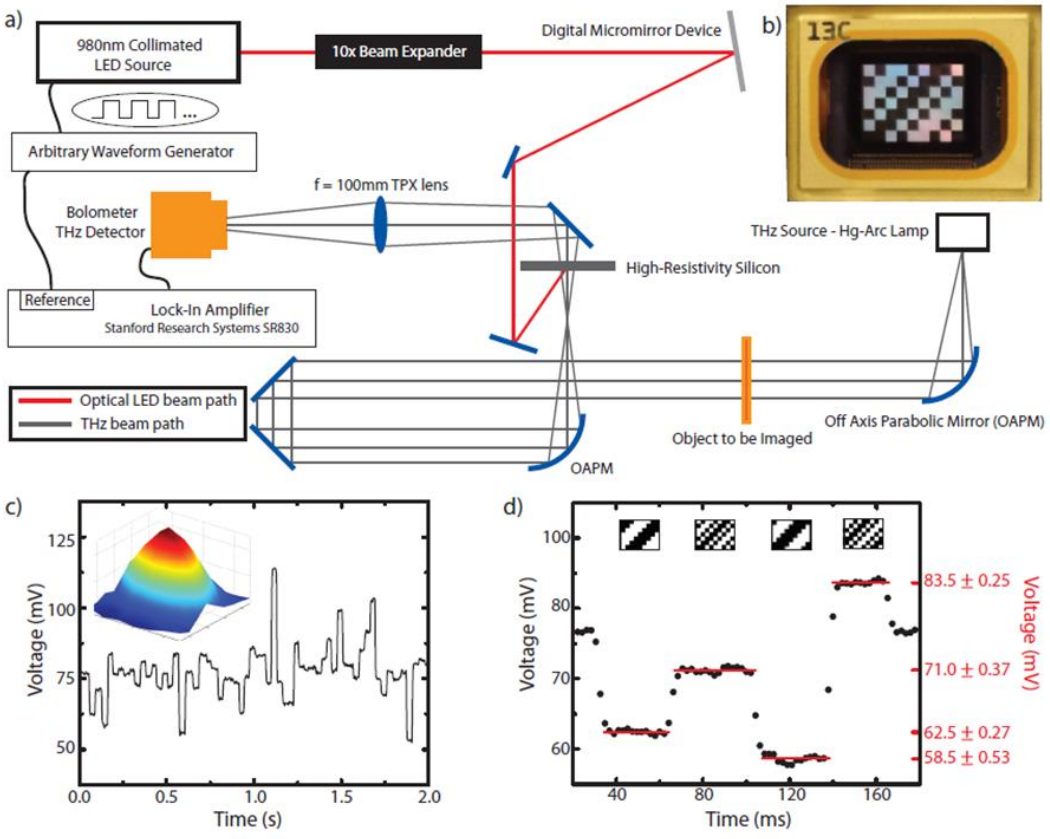

Fig. 4.2 – Imaging Apparatus (a) Schematic of LED and THz optical layouts. The THz beam (shown in gray) passes through the object and is imaged with the OAPMs onto a ρ -Si wafer. The collimated 980 nm wavelength optical beam (shown in red) reflects off the DMD surface and creates a spatial light pattern at the THz image plane. (b) Photograph of a 7×9 S-matrix mask pattern displayed on DMD; each mask pixel is 1.5 mm being constructed from tiling 109 × 109 DMD pixels. (c) Lock-in amplifier voltage output is displayed as a function of time in seconds for the 63 sequential S-matrix masks; the entire measurement takes approximately 2 s. Inset: reconstructed THz beam profile at image plane. (d) Zoom-in of time data shown in (c). Raw data from four consecutive S-matrix mask measurements are shown with the corresponding binary mask shown above; the averaged values used for reconstruction along with the standard deviation are shown on the right.

4.3.2 Digital Micromirror Device and Optical Modulation

An optical beam is used to spatially modulate the THz image and consists of a 2 W multimode laser diode at a wavelength of 980 nm. An aspheric lens collimates the laser and a Galilean beam expander is used to produce a beam which slightly overfills the DMD. Light is reflected from the DMD in the blaze configuration (described below) and the spatially patterned optical beam is aligned to overlap with the THz image at the front surface of the ρ-Si wafer achieving a maximum optical fluence of 250 mW/cm^2. The DMD shown in Fig. 4.2 (b) is utilized to spatially modulate the optical beam by configuring it as a blazed diffraction grating. Our DMD (DLP D4100-2XLVDS) has a window optimized for the transmission of NIR and 1024 ×768 micro-mirrors (total area 14.0 mm × 10.5 mm), where each mirror has a pitch d_{DMD} = 13.68 μm and behaves as a binary reflector. By aligning the angle of incidence correctly, the majority of the energy can be directed into the "blazed" order [116]. The blazed condition for the wavelength λ_B is related to the grating pitch $d = \sqrt{2}d_{DMD}$, the diffraction order m, and the facet angle φ = 12° as shown in Eq. 4.3. The fourth blazed angle is centered at λ = 984 nm with an efficiency of 47% [117].

$$\lambda_B = \frac{d}{m}\sin 2\phi \tag{4.3}$$

The DMD is computer controlled and able to change between frames up to a (software limited) time of 32 ms. Binary bitmap files are loaded into the software to be displayed on the DMD. The white portions represent light that was directed toward the ρ -Si whereas black represents light that was directed away. This corresponds to white mask regions photodoping the ρ -Si, i.e. modulating the THz transmission where black represents unmodulated regions. Since the DMD is designed for much shorter optical wavelengths, we may utilize several mirror pixels to function as a single THz-sized pixel for the S-matrix mask, thus permitting flexibility for both pixel count and pitch. We use S-matrix masks of varying complexity and change the pixel size

accordingly to keep the overall mask area approximately equal. The THz image resolutions we investigated are summarized in Table 4.1 and the relation between physical size and DMD pixels is detailed.

4.4 Results and Discussion

Order (N)	Resolution	THz Pixel Size	DMD Pixels / THz Pixel
63	7×9	1.5 mm × 1.5 mm	109×109
255	15×17	698 μ m × 698 μ m	51×51
1023	31×33	328 μ m × 328 μ m	24×24

Table 4.1 Relationship between THz imaging resolution and DMD pixel sizes

Using the experimental apparatus shown in Fig. 4.2 we performed single pixel THz imaging of various scenes. All THz images are normalized by referencing to the beam profile with no object present. The flexibility afforded by our setup enabled us to image at many different mask resolutions and sizes without physically changing the system. Figure 4.2 (c) shows the THz signal for 63 different S-matrix masks displayed over a period of 2 s (each mask is displayed for approximately 32 ms). Figure 4.2 (d) shows zoomed-in raw data for consecutive S-matrix masks, with the corresponding binary mask shown above and the average value used for reconstruction shown in red on the right axis. The inset to Fig. 4.2 (c) shows a false color image of the THz beam profile at the image plane. The reconstruction was done using 63 measurements from the 7 × 9 S-matrix masks (pixel size 1.5 mm) with the total measurement time of approximately 2 s. It is clear from the data shown that quality THz images can be acquired in relatively short times. As stated, the current limitation on speed was software related resulting in mask modulation speed of approximately 31 Hz. However, the response time of the system to a change in mask is approximately 5 ms, resulting in a potential frame rate of 3 fps.

In order to compare our imaging system to more conventional schemes, we perform both raster scan and Hadamard imaging and highlight differences between the two methods – see Fig.

4.3. S-matrix masks consist of roughly 50% light throughput and it has been demonstrated that using masks from an $N \times N$ S-matrix can increase SNR by a factor of $\frac{(N+1)}{2\sqrt{N}} \cong \frac{\sqrt{N}}{2}$ over raster scan imaging with the same resolution and pixel size [97]. Figs. 4.3 (a), 4.3(b) show both the metallic aperture used as an object and an optical photograph of the conjugate image at the front surface of the ρ-Si wafer. It is well known that aspheric optics, such as OAPMs, produce aberrations that can distort the image plane in the form of astigmatism and coma, as seen by the image distortion in Fig. 4.3 (b) [118].

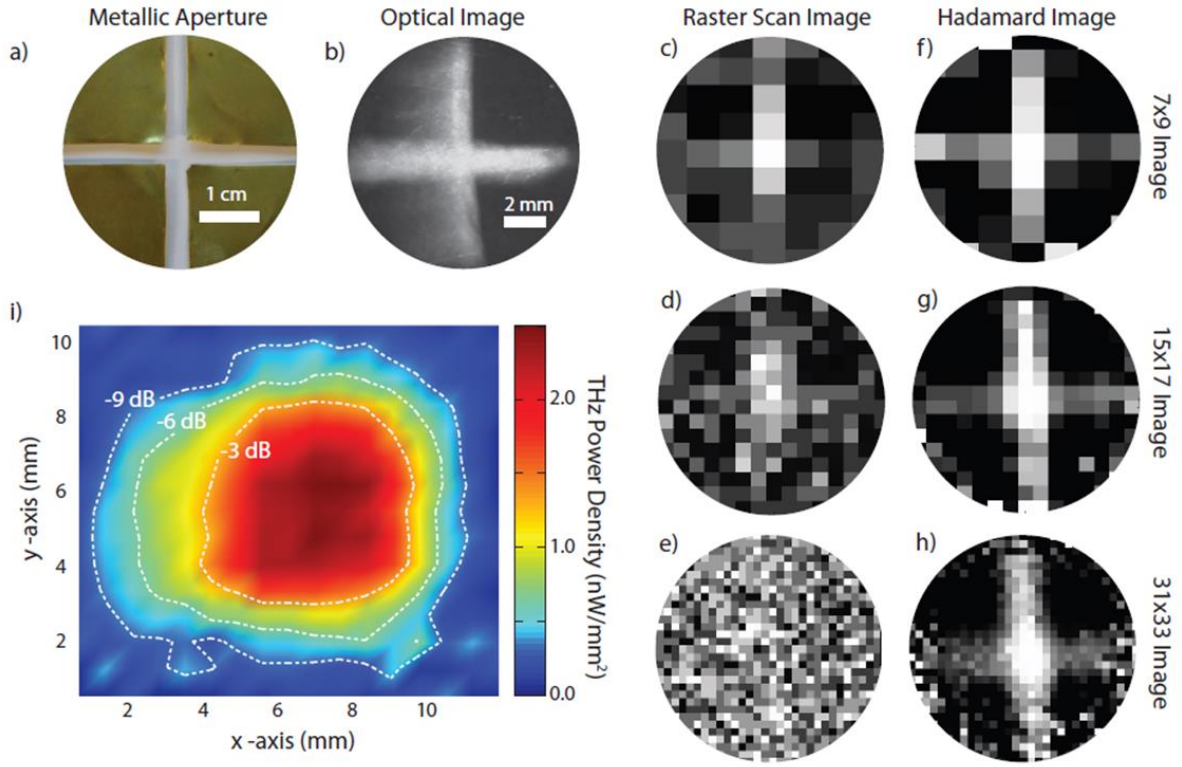

Fig. 4.3 – Imaging with Various Measurement Matrices Comparison of THz imaging with raster scan masks and S-matrix masks. (a,b) Show the metallic aperture used as the object and the conjugate optical image on the ρ -Si wafer. (c) - (e) Shows raster-scan images for increasing mask complexity. (f) - (h) Shows Hadamard reconstructed images of the same size and complexity as the raster scan measurements to the immediate left. Each mask was displayed for 500 ms for all above measurements. (i) Spatial map of the THz power density shown for the reference beam profile with contour plots showing the intensity drop in dB.

Figures 4.3 (c) – 4.3 (e) show raster-scan images acquired with increasing resolution and constructed from 63, 255, and 1023 measurements respectively. The last column in Fig. 4.3 (f) – 4(h) shows Hadamard reconstructions with the same number of measurements and resolution as the raster scan images. In order to compare different imaging techniques and resolutions, an identical time of 500 ms per mask was used, giving total acquisition times of 31.5 s for the 7 × 9 images, 127.5 s for the 15 × 17 images, and 511.5 s for the 31 × 33 images. While the image quality in the case of 7 × 9 pixel resolution is comparable between the two techniques, the rapid decrease in image quality for the raster scan images at higher resolutions is apparent - see Fig. 4.3 (e). In contrast, the image quality is retained for increasing pixel count in the multiplexing case.

To better understand why the signal depreciated significantly for increasing pixel complexity in the case of the raster scan we investigated the measured power for each respective mask type. We calculate the spatial dependence of the power density ($\mathrm{nW/mm^2}$) by taking the total measured THz power (96 nW) and extracting the THz power density per pixel p_i from the measured 15×17 beam profile intensity as defined by

$$p_i = \frac{96\mathrm{nW}}{(698\ \mu m)^2} \times \frac{x_i}{\sum_{i=1}^{255} x_i}, \tag{4.4}$$

where x_i is the reconstructed signal from pixel i. In Fig. 4.3 (i) we show a high quality image of the power density - sufficient to observe optical aberrations resulting from the use of OAPMs which result in an asymmetric distribution of THz power about the horizontal axis, as mentioned above. The power/pixel decreases for increasing resolution since the pixel size is reduced - in our case from 1.5 mm to 698 μm to 328 μm. The peak power density calculated in Eq. 5 is 2.5 $\mathrm{nW/mm^2}$ near the center of the beam. This corresponds to a total of 5.6 nW of measured power for the 1.5 mm size pixel and 0.27 nW for the 328 μm pixel, a 95% reduction of measured power proportional to the decrease in pixel area. As shown in Fig. 4.3 (i), the power density is -9 dB lower towards the outer diameter of the images and approaches values as low as 50 pW of THz

power for 328 μm sized pixels - still well above the bolometer's specified noise-equivalent-power (NEP) of 1.57×10^{-13} W/ Hz. The raster scan is unable to compensate for the loss in measured signal for each pixel due to decreasing pixel dimension. In the Hadamard case, although the signal per pixel also drops with decreasing pixel size, the increase in sampled pixels for each data acquisition offsets the reduction in signal. Consequently, the higher resolution image offers more information without sacrificing SNR. The improvement in the image quality for increasing pixel complexity is evident and allows for the aberrations of the THz image resulting from the OAPMs to be rendered.

In order to explore our imaging technique for possible use in screening applications, in Fig. 4.4 we show various examples of high-fidelity THz images. The top row displays photographs of all the objects imaged: crosses with 8 mm and 4.5 mm wide arms at the object plane (Fig. 4.4 (a), 4.4 (b)) and two razor blades imaged in manila envelopes (Fig. 4.4 (c), 4.4 (d)). As stated above, we can program the S-matrix masks to allow for several different functions and mask complexities.

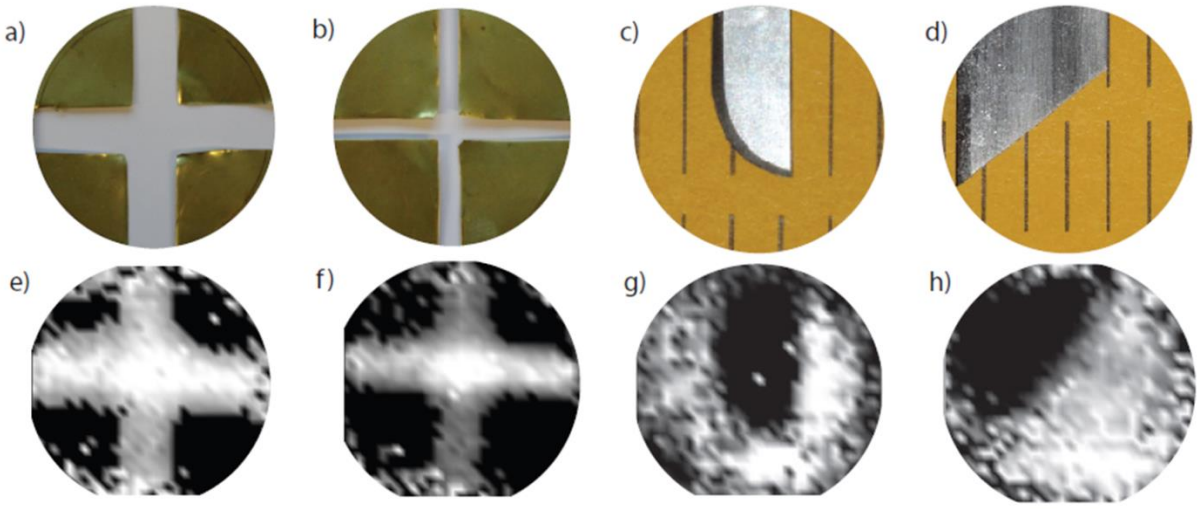

Fig. 4.4 – Imaging Optically Hidden Objects THz imaging with high-resolution S-matrix masks (31 × 33 pixels with each pixel measuring 328 μ m on a side). (a, b) Show metallic apertures used as the object of two differently sized crosses, with arm widths of approximately 8 mm and 4.5 mm in the object plane mapping to 2.5 mm and 1.5 mm on the image plane. (c, d) Two different types of metal razor blades that were placed in manila envelopes for imaging. (e) - (h) Shows the THz images of the corresponding objects shown immediately above. Each mask was displayed for 500 ms for all measurements above, giving a total acquisition time of 511.5 s for each image.

We achieved high resolution images containing 31 × 33 pixels with each mask pixel measuring 328 μ m across; this was acquired with 1023 sequential measurements. Like the images shown in Fig. 4.3, the masks were displayed for 500 ms each, giving a total image acquisition time of 511.5 s. The reconstructed THz images are shown in Fig. 4.4 (e) – 4.4 (h). Due to the magnification of the system, the crosses are imaged down to have 2.5 mm and 1.5 mm wide arms, respectively. The minimum feature size of the images that we can resolve for these crosses is limited by diffraction. The Rayleigh criterion suggests we achieve a diffraction limited spot size of approximately 1.4 mm at 1 THz, although the inherently broadband nature of detected radiation presented here generates a more complex diffraction pattern than that for use of a monochromatic source [119]. The razor blades are placed within manila envelopes and are, obviously, not visible in the optical, however are clearly identified in the THz images, demonstrating the potential for THz imaging to be used in security applications.

4.5 Conclusion

We have performed high fidelity THz single pixel imaging and various scenes have been rendered. An optically controlled spatial light modulator was implemented through photodoping in high resistivity silicon and controlled by a DMD. We use S-matrix masks of varying resolution ranging from 63 to 1023 pixels and were able to obtain THz images as fast as one per two seconds. We directly compared Hadamard imaging to the raster-scan technique and highlighted the advantages of the multiplexing method. At THz frequencies dynamically reconfigurable semiconducting device technology provides significant advantages over traditional masks due to the benefit of adaptability and real-time control. In the next chapters, we will show additional implementations of single pixel imaging systems at longer wavelengths that utilize similar techniques.

5. Electronically Controlled MM-SLM for Single Pixel THz Compressive Imaging

5.1 Introduction

Much like in the last chapter, where we utilized optical pumping of a semiconductor to change its optical properties, here we utilize a bias voltage to deplete carriers from a semiconductor. This GaAs layer is integrated into our MM structure, so by modulating its optical properties we modulate the MM properties as a whole.

We now discuss implementation of a single pixel imager, again in the THz regime, using an electronically controlled dynamic MM-SLM. The imaging apparatus is very similar to that used in chapter 4 (the same THz source and detector were used), and the theory is the same. Below we show that the electronically controlled SLM makes the system efficient enough to image at a frame rate of 1 fps. Before discussing the imaging capabilities, we explore extensively the physical mechanism behind the THz modulation.

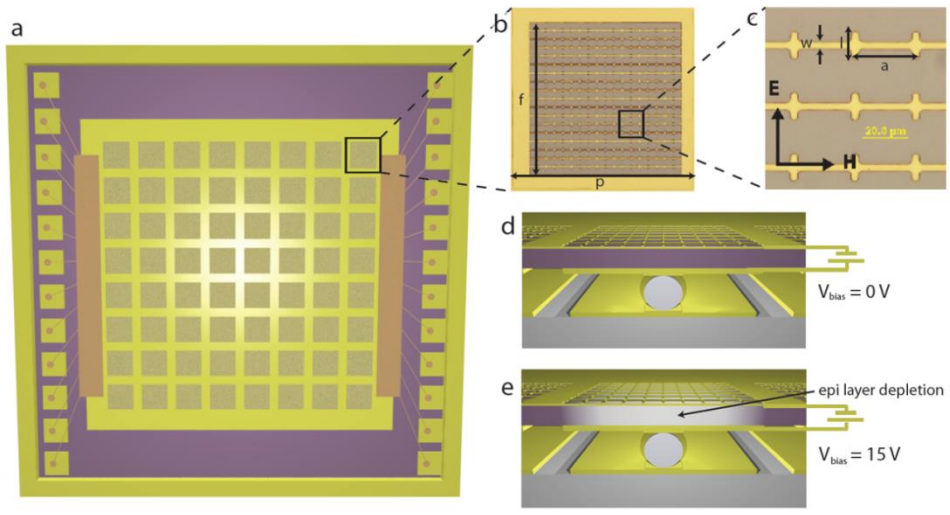

Fig. 5.1 – Metamaterial SLM Design (a) Top view of 8 × 8 SLM comprised of metamaterial perfect absorbers. (b) Photograph of a single pixel, made from an 18 × 18 array of MMA unit cells with dimensions (in μm): p = 600, f = 486. (c) Several MMA unit cells with dimensions (in μm): w = 3, l = 15.2, a = 27. Side view of SLM in the (d) non-depleted and (e) depleted states.

5.2 Experimental Details

5.2.1 SLM Device

In our design, shown in Fig. 5.1, we utilize an electronically controlled 8 × 8, mask where each pixel is comprised of dynamic, polarization sensitive MMAs. The electromagnetic properties of the metamaterial can be tuned through an applied bias voltage and thus each of the 64 pixels is individually and dynamically addressable, permitting operation as a real-time spatial mask for THz radiation.

Absorption modulation is achieved by applying a reverse bias voltage between the resonant top layer (acting as the Schottky contact) and the ground plane (acting as the Ohmic contact), schematic shown in Fig. 5.1. The reverse bias depletes the epi-layer underneath the cut wire array, lowering the carrier concentration in the dielectric layer. The change to the carrier concentration alters both the real and imaginary part of ε_{GaAs} which, in turn, modulates both the frequency and amplitude of the absorption peak, respectively. This effect was simulated and found to be consistent with the experimental results [20].

5.2.2 SLM Performance

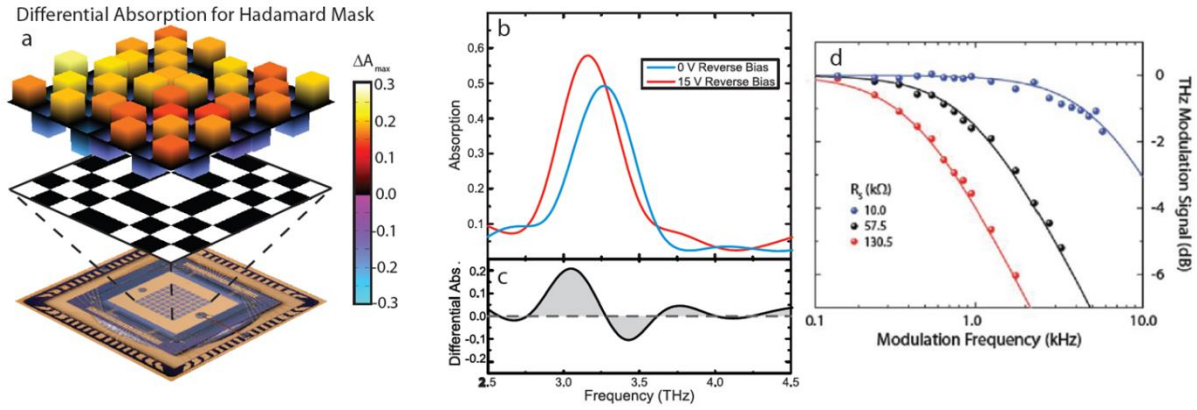

Fig. 5.2 – SLM Performance (a) Spatial map of maximum differential absorption for an example Hadamard mask over photograph of SLM device. Colorbar gives maximum differential absorption for that pixel. (b) Frequency dependent absorption of a single pixel (referenced to a gold mirror) for two bias voltages, 0 V reverse bias (blue curve) and 15 V reverse bias (red curve). (c) Differential absorption ($A_{15V} - A_{0V}$) as a function of frequency. (d) Signal roll-off as a function of modulation frequency for several different series resistors.

The sample performance was characterized in several ways. In Fig. 5.2(a) we display the experimental differential absorption (ΔA_{max} = (mask value)×$|A_{15V}(\omega)-A_{0V}(\omega)|_{max}$) for a characteristic coding mask where we evaluate mask values that may be 0, +1 or -1. In Fig. 5.2(b) and 5.2(c) we show the absorption and differential absorption, respectively, for a characteristic metamaterial pixel as a function of bias voltage.

Additionally, current-voltage curves were measured to determine the most optimal operating voltage. The device was found to perform best below -26.5 V [20]. Additionally, the sample was characterized as a function of modulation speed. Past SLM devices, such as liquid crystal based samples, perform best at modulation speeds on the order of 1 kHz [120]. An SLM with increased modulation speed could decrease image acquisition time by lowering the time each mask is displayed on the SLM. The SLM effective *RC* time constant was determined by loading the sample with several external series resistors and obtaining the effective device capacitance, shown in Fig. 5.2(d). The 3 dB roll-off frequency (i.e. the characteristic maximum modulation frequency) was found to be 12 MHz [20]. The increase in modulation speed over similar designs [121] stems from the Ohmic ground plane being directly underneath the Schottky layer, reducing the device capacitance. The electrical cross talk was also measured on the SLM device. A single pixel was modulated with a function generator between 0 V – 10 V and the resulting signal was measured with the lock-in amplifier across nearest neighbor pixels. At the modulation frequencies used to take data, the cross talk was negligible with an instrumentation noise floor of approximately -70 dB.

5.2.3 Imaging Apparatus

Like the imaging apparatus described in chapter 4, the source is a 5500 K blackbody Hg-arc lamp; the same filter is used. Two 90° off-axis parabolic mirrors with diameter and effective focal length of 101.6 mm and 152.4 mm respectively are used to illuminate the object and project an image of the object on the SLM. A toric mirror and off axis parabolic mirror are used to focus the spatially modulated image onto the single pixel detector. The distance from the object to the

imaging off axis parabolic mirror (OAPM) is 940 mm; the distance from the imaging OAPM to the SLM is 178 mm, giving a system magnification of 18.9%. We use a liquid-He cooled silicon bolometer as our intensity based single pixel detector (same as chapter 4).

The SLM is housed on a 15 V powered PCB with 64 individual transistors. Signal is sent from a field programmable gate array (FPGA) to control each pixel; the signal from the FPGA is modulated *via* a function generator. In order to quantify the electronic performance of our SLM we performed cross talk measurements, but were unable to measure any signal with an instrument noise floor of -70 dB. One of the connections to the FPGA was damaged on the PCB, causing that pixel to not modulate (row, column = (1, 6)). The SLM sample has two shorted pixels (row, column = (4, 7) and (4, 8)); this gives a total yield of 61 out of 64 on the device. We use a lock-in amplifier (Stanford Research Systems SR830) to process the modulated radiation detected by the bolometer. Our measured signal is proportional to the integrated differential absorption shown as the shaded region in Fig. 5.2(c), producing a measured power of 1.17 nW for that single pixel. Additionally, we only sample approximately half the pixels per measurement when using the Hadamard masks, resulting in a total average measured power of 34 nW. For Fig. 5.3 and 5.4 the pixels were modulated from 0 to -15 V at 199 Hz with an integration time τ = 300 ms on the lock-in amplifier; for Fig. 5.5 the pixels were modulated at 401 Hz with τ = 3 ms.

5.2.4 Novel Modulation Scheme for Achieving Negative Mask Values

It is widely believed that intensity-based imaging systems require mask values which are confined to be either 1 or 0, as physical masks may either pass light to the detector or block it. However, utilization of masks with negative values yields lower noise [97], but is generally only achievable with phase sensitive measurements. Often intensity-based imaging masks are approximated by collecting two [1, 0] masks and subtracting them, i.e. obtaining a mask with [1, 0, -1] or [1, -1] values [122]. However, there are two significant disadvantages to the above approach – twice as many measurements are necessary, thus doubling acquisition time, and the noise power increases as the variance is additive [123]. Here we introduce a technique that

utilizes a lock-in detection scheme permitting imaging with [1, -1] or [1, 0, -1] mask values directly. In our approach, +1 (-1) pixels are modulated in phase (out of phase) with a reference.

Modality	**# Meas.**	$\Phi = M \times N$	**Mask Values**	**MSE at P_T = 0.15 nW**	**Compression**	**Figure**
Raster Scan	64	64×64	[1, 0]	0.531	None	5.3a
Random	64	64×64	[1, 0]	0.156	None	5.3b
Random	128	64×64	[1, 0, -1]	0.109	None	5.3c
Random	128	128×64	[1, 0]	0.031	None	5.3d
Hadamard	64	64×64	[1, -1]	0	None	5.3e
Hadamard – Sequency	64	64×64	[1, -1]	--	None	5.4a
Hadamard – Sequency	51	51×64	[1, -1]	--	79.7%	5.4b
Hadamard – Sequency	38	38×64	[1, -1]	--	59.4%	5.4c
Hadamard – Sequency	33	33×64	[1, -1]	--	51.6%	5.4d
Hadamard – Sequency	19	19×64	[1, -1]	--	29.7%	5.4e

Table 5.1 Description of different mask modalities used for the imaging data seen in Figs. 5.3 and 5.4. 'Modality' describes the types of masks displayed on the SLM, '# Measurements' describes the number of measurements used to reconstruct the image, '$\Phi = M \times N$' describes the size of the measurement matrix where M is the number of measurements and N is the number of pixels (N = 64), 'Mask Values' gives the values of which each measurement matrix Φ was comprised. 'MSE at PT = 0.15 nW' describes the normalized Mean Square Error evaluated at a threshold power of 0.15 nW for reconstructions shown in Fig. 5.3. 'Compression' gives the ratio of number of measurements taken (M) to the total number of pixels (N = 64). 'Figure' gives the location of the reconstruction.

5.3 Imaging Results

We explore various measurement matrices, both for their signal-to-noise ratio and image quality benefits. Specifically, we compare traditional masks comprised of a binary [1, 0] (intensity based) set to those utilizing negative values, i.e. chosen from a [1, 0, -1] or [1, -1] (phase based) set. Table 5.1 lists the various mask modalities used to image an inverse cross (see

Fig. 5.3(a) – 5.3(f)). Remarkably, despite the fact that our scene is only illuminated with a total power [124] of 67 nW, high quality images are evident. We note that imaging with Hadamard masks (Fig. 5.3(e)) results in the best qualitative images, even when compared to Fig. 5.3(d) in which twice the number of samples are used to reconstruct the image.

5.3.1 Benefit of Negative Mask Values

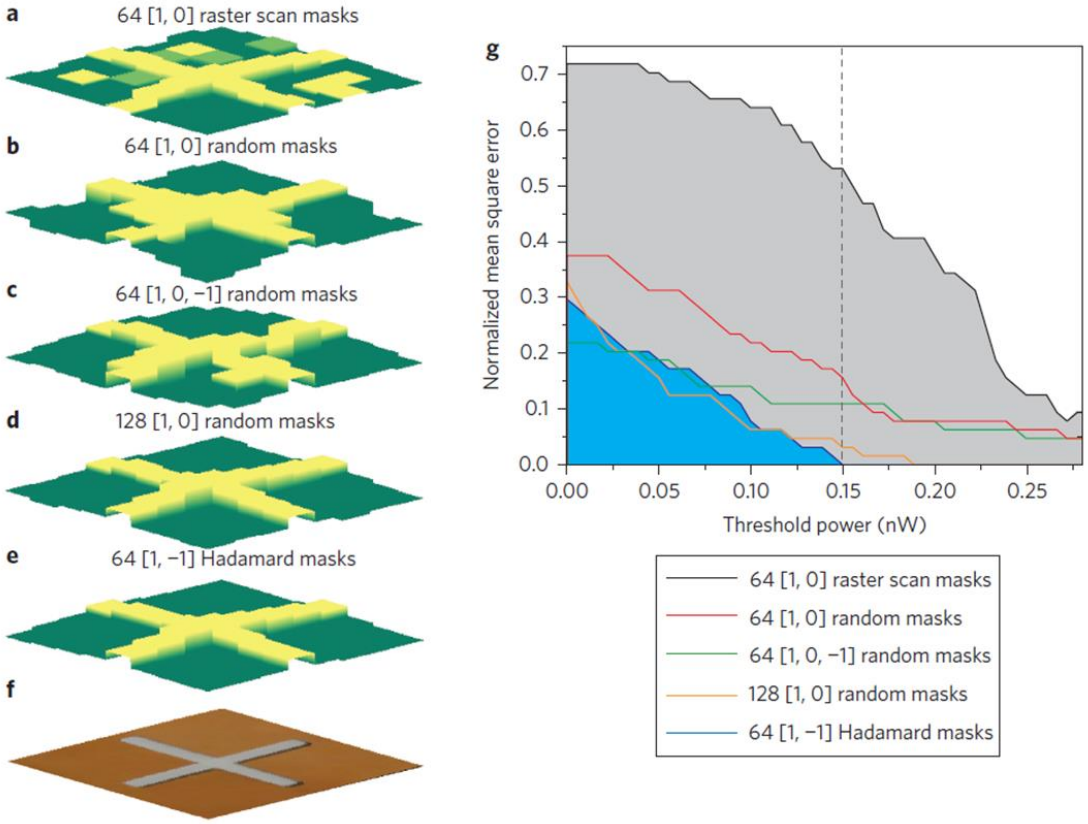

Fig. 5.3 – Imaging with Various Measurement Matrices Inverse cross reconstructed with (a) 64 [1, 0] raster-scan masks, (b) 64 [1, 0] random masks, (c) 64 [1, 0, -1] random masks obtained by subtracting 2 sets of data, (d) 128 [1, 0] random masks, and (e) 64 [1, -1] Hadamard masks. (f) Photograph of object (inverse cross). All reconstructions are plotted on the same color axis. (g) Calculated normalized mean square error for various reconstruction methods as a function of binary threshold power (P_T) (in nW), as defined in the text. Dotted line drawn at $P_T = 0.15$ nW is used to compare MSE values between different coding methods.

Although the benefit of using phase contrasted masks for single pixel imaging is visually evident, we can perform image analysis permitting a quantitative account of this advantage. In

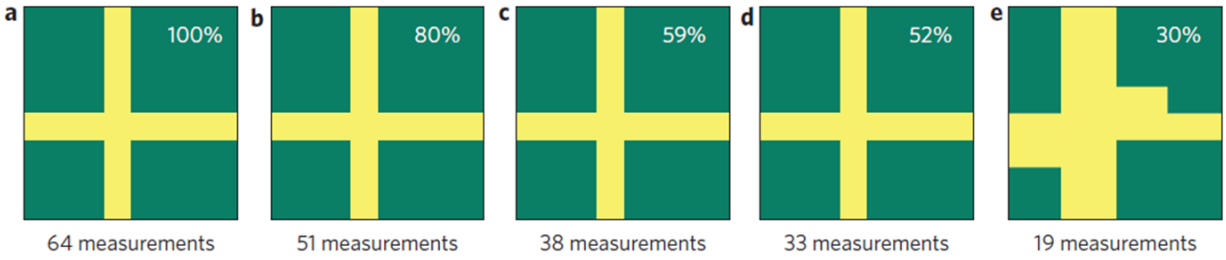

Fig. 5.4 – Compressive Imaging Measurements Reconstructed images of inverse cross with 64, 51, 38, 33 and 19 measurements shown in (a) – (e), respectively. The colormap scale of each reconstruction was chosen to best display the data.

Fig. 5.3(g) we show the normalized mean square error (MSE) calculated as the difference between the reconstructed binary image versus the object. The MSE is plotted as a function of binary threshold power (P_T), i.e. all values greater than P_T are treated as a 'one' and all equal to or less than are treated as a 'zero'. Notably, this analysis confirms that direct access to negative pixel values, as seen in the Hadamard phase encoding scheme demonstrated here (solid blue curve), yields an MSE of 0 at the lowest P_T of 0.15 nW, followed by the imaging with 128 random intensity based masks. Other encoding schemes do not achieve a perfect image rendering, see Table 5.1 for results.

5.3.2 Compressive Imaging

Having demonstrated single pixel imaging we next show that THz images may be obtained with compressive methods. As stated in chapter 3, there are well developed mathematical techniques to reconstruct X from an underdetermined equation $Y = \Phi X$, i.e. reconstruct a 64-element image with less than 64 measurements or $M < N$. Here we use a sequency ordered [97] partial Hadamard matrix as Φ. The inverse cross, shown in Fig. 5.3(f), was imaged and reconstructed using the fast-iterative shrinkage thresholding algorithm (FISTA) [107, 125]. Figures 5.4(a) – 5.4(e) show results with various compressions (see Table 5.1). The cross image is maintained fairly well for most values of compression, even when the number of measurements is compressed by over a factor of 3, as in Fig. 5.4(e).

5.3.3 Imaging a Moving Target

In single pixel imaging the speed of acquisition is directly proportional to the number of samples required for image reconstruction. Utilization of compressive techniques reduces the number of acquisitions necessary, thus decreasing imaging time. In Fig. 5.5(a) an object (see Fig. 5.3(f)) was imaged with 64 Hadamard phase masks, each shown for 22.4 ms, giving a total acquisition time of 1.43 s. If we 'compress' the number of measurements and only collect the first 45 measurements (as shown in Fig. 5.5(b)), the image acquisition time may be further reduced to 1.00 s with little impact to image fidelity. Continuous image acquisition would then give a THz frame rate of 1 Hz – far faster than many traditional raster-scanning techniques, which are limited to about 0.15 – 0.3 Hz (10 – 20 pixels per second) [88].

In order to test the viability of our compressive setup to achieve 'real-time' operation, we perform imaging of a moving object. An inverse cross (shown in Fig. 5.5(c)) was moved laterally across the scene at 1.8 mm/s. We collected 10 continuous frames at 70% compression, i.e. 450 sequential masks with each displayed for 22.4 ms. The moving object was reconstructed using FISTA and the first five frames are shown in Fig. 5.5(d) (see Attached Movie 5.1). The cross

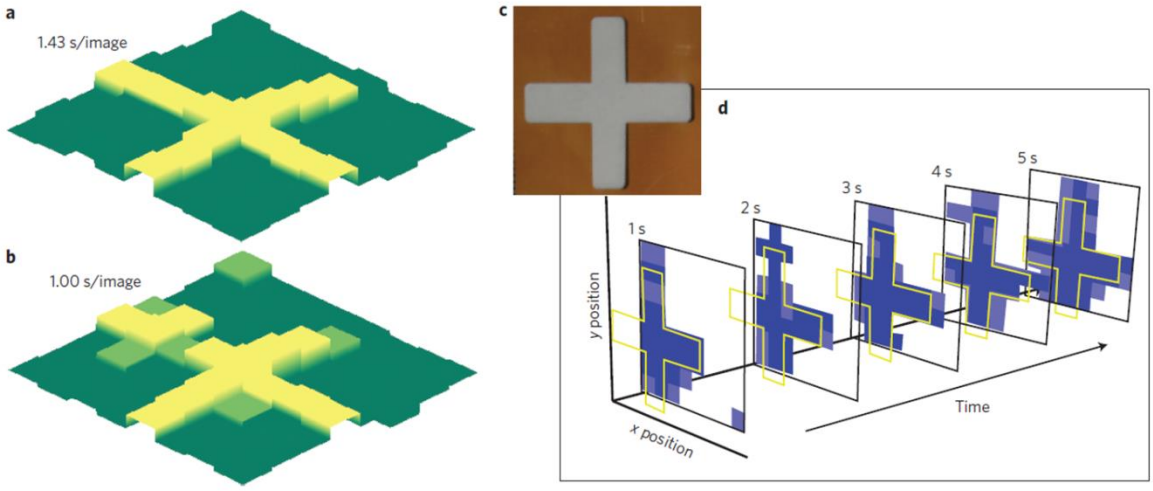

Fig. 5.5 – Increase in Image Frame Rate (a) Image reconstruction using 64 masks with each mask displayed for 22.4 ms giving a total image acquisition time of 1.43 s. (b) Image reconstruction using FISTA and 45 masks with each mask displayed for 22.4 ms giving a 1 s total image acquisition time. The colormap scale of each reconstruction was chosen to best display the data. (c) Photograph of object used for study. Object was scanned across field of view at speed of 1.8 mm/s. (d) Consecutive tiles show FISTA reconstruction using 45 Hadamard masks. Only the first 5 frames are shown in the figure, see Supplementary Information for full video (10 frames). The approximate position of the cross aperture is shown in yellow as a guide to the eye.

shape, shown in blue, can clearly be seen moving across the transparent background as time progresses.

5.4 Conclusion

In this chapter, we have presented both single pixel Hadamard and single pixel compressive imaging in the THz regime. Design and fabrication of an all-electronic, reconfigurable, polarization sensitive metamaterial SLM enabled demonstration of low-noise, high fidelity multiplex imaging, despite use of an extremely low power THz source. Compressive sensing techniques further allowed for an increase in frame rate by 43%, thus permitting imaging of a moving object. This same MM-SLM is used for experiments described in chapter 7, where we implement novel telecommunication techniques into the THz single pixel imager.

6. Passive, Frequency Diverse MM-SLM for Millimeter Wave Imaging

6.1 Introduction

In chapters 4 and 5, we discussed the merits of single pixel cameras, collecting spatially multiplexed measurements in time to reconstruct a scene. This method does, indeed, have many benefits over inefficient raster scan imaging systems or expensive detector arrays at longer wavelengths. We were able to efficiently reconstruct images (see Figs. 4.3, 4.4, 5.2, and 5.3) and were able to take steps to push the frame rate to 1 fps (Fig. 5.4). However, even with the strides made in single pixel imaging, the designs still have the drawback that the measurements must be taken serially in time. The higher resolution of the image, the more encodings must be used, hence resulting in an increase image acquisition time. This serial measurement technique could be avoided if the spatial information were encoded in a different dimension rather than time. If spatial masks were each encoded in a frequency band, a single, passive, frequency dependent SLM could be used instead of an active SLM. Then, rather than recording the signal from each encoding mask serially in time, one could take a single, hyperspectral measurement to gain the same amount of information.

Frequency information has been used to gain spatial information previously in a proof of concept design using a grating to physically separate the light into different frequency bands [126]. In this chapter we explore metamaterials as a means to create a completely passive, frequency dependent SLM. We present the implementation of a single pixel camera in the mm-Wave regime and use metamaterial technology to create a totally passive SLM that uses frequency diversity to gain spatial information from a mm-Wave scene. We were able to display several encoding masks, each embedded in a frequency rather than in time, and using compressive sensing techniques, were able to reduce image acquisition time to 6 fps.

6.2 Experimental Details

6.2.1 Millimeter Wave Apparatus

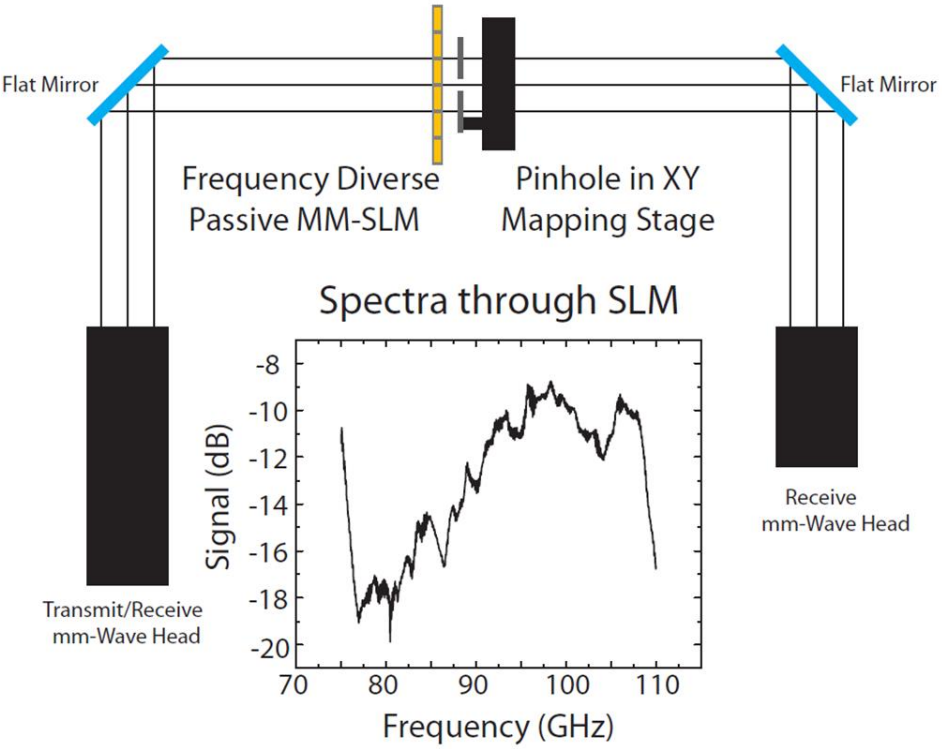

Fig. 6.1 – Millimeter wave imaging schematic. Pinhole maps out the measurement matrix ($\boldsymbol{\Phi}$) determined by the spectra passing through each pixel of the SLM. The pinhole mapping plane is replaced with an object ($\boldsymbol{X}$) to be reconstructed. A single hyperspectral measurement ($\boldsymbol{Y}$) is then collected to reconstruct the object.

The imaging apparatus is shown in Fig. 6.1 and consists of an Agilent PNA-X vector network analyzer for 2-port radiation source and detection. Millimeter wave head extenders were used to extend the bandwidth of the VNA into the W-band (75 – 110 GHz). Collimated light from the lens-horn is incident on the passive SLM, where each spatial pixel is encoded with a characteristic spectral response. This spatial/spectrally encoded wave front then passes through the millimeter-wave scene (a flat metallic aperture milled out with various shapes). The resulting radiation is then collected as a hyperspectral measurement.

Equating the above components to the generalized single pixel imaging apparatus in Fig. 3.2 and the imaging theory in chapter 3, we can consider the mask to be encoding masks not in

time, but in frequency. Therefore, the rows of the experimental measurement matrix, or spectral measurement matrix, Φ_s, are frequency points rather than masks in time. The spectral measurement vector, Y_s, represents spectral components, rather than measurements in time. The mathematical theory will be identical, and the scene can be reconstructed with the same methods.

6.2.2 SLM Device

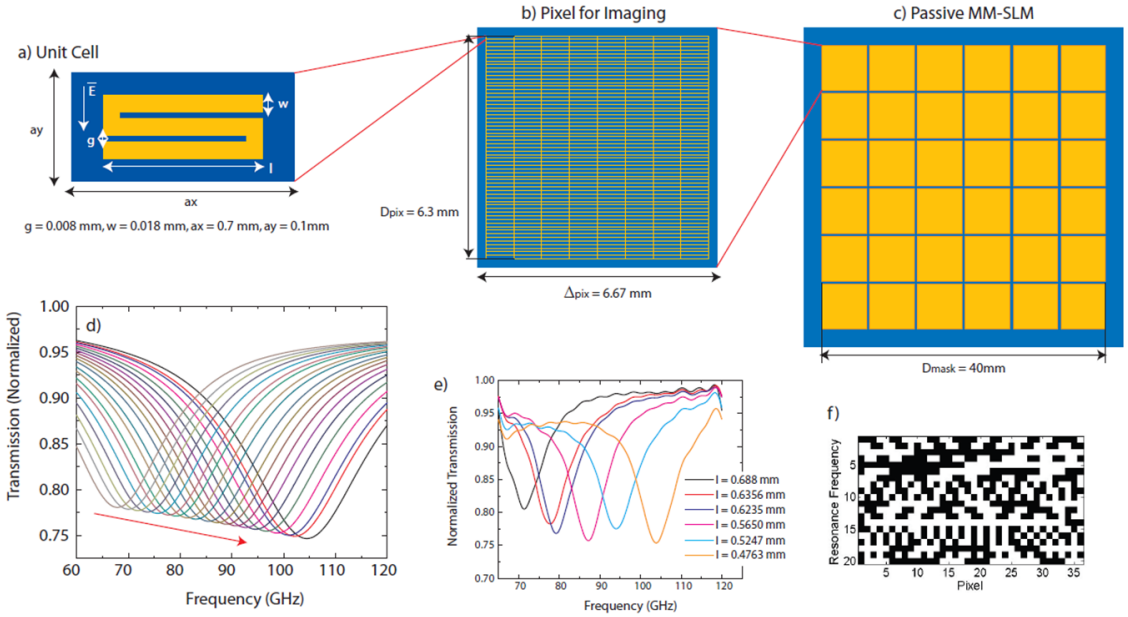

Fig. 6.2 – MM-SLM Metamaterial spatial light modulator components. (a) Single unit cell with parameters listed. The width of the structure (l) determines the resonance frequency. (b) Each imaging pixel is made of several different types of unit cells to give it a multi-frequency response. (c) Each pixel is then a spatial component of the 6x6 SLM. (d) Simulated transmission values for each of the 20 different types of unit cells used in the SLM from l = 0.48 mm to l = 0.705 mm. The red arrow denotes decreasing values of l. (e) Experimentally measured transmission values for several different types of unit cells. (f) Design of binary measurement matrix implemented on SLM. Each column represents a pixel, while each row represents a type of unit cell (represented by a curve in (d)).

Starting from the unit cell level, our SLM device was comprised of a polarization-sensitive, gold meander-type metamaterial on a 500nm SiN window (shown in Fig. 6.2(a)). This type of unit cell, when patterned in an array, will have high transmission with a minimum at some resonant frequency. The critical parameter was the length of the meander (l) and determined the transmission minimum.

Each pixel (Fig. 6.2(b)) was composed of many different types of unit cells to give a characteristic multi-frequency response. The SLM we implemented had 6×6 (N = 36) pixels (see

Fig. 6.2(c)) and utilized $M = 20$ different types of unit cells, with the simulated transmission values shown in Fig. 6.2(d), where the red arrow denotes decreasing length parameter l. A test sample was made in which arrays contained just a single type of unit cell; measurements from this test sample are shown in Fig. 6.2(e).

The measurement matrix (20×36 binary matrix shown in Fig. 6.2(f)) was taken from a 63x63 S-matrix. Each row represents a specific unit cell length, or characteristic transmission minimum. The columns represent the pixels of the mask: 1 (white) denotes that the unit cell for that frequency is present in that pixel, 0 (black) denotes its absence. Each imaging pixel contained approximately 600 unit cells and had filling fractions for each pixel ranging from 1/8 to 1/14.

6.3 Results and Discussion

6.3.1 Measurement Matrix

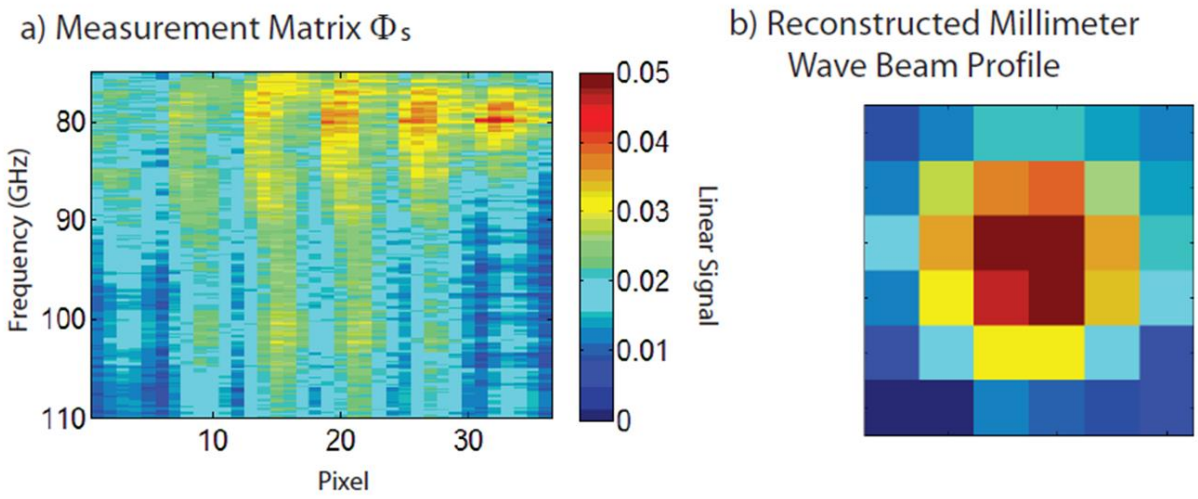

Fig. 6.3 – Imaging Measurements (a) Measurement matrix used for reconstruction. (b) Reconstructed millimeter-wave beam profile.

The spectral measurement matrix, Φ_s, was experimentally measured in order to best reconstruct the scene. This was done by raster-scanning a pixel-sized pinhole (cut out of a

metallic aperture) across field of view (FOV) of the frequency diverse spatial light modulator. A transmission spectrum was gathered at each spatial position, and collected into a spectral measurement matrix. Rather than the 36×20 measurement matrix shown in Fig. 6.2(f), the number of rows in Φ_s is determined by the frequency resolution. A sample measurement matrix is shown in Fig. 6.3(a) where we have used 1001 frequency points from 75 – 110 GHz.

6.3.2 Imaging Experiment

A single, hyperspectral measurement was taken of the millimeter-wave beam, also with 1001 frequency points (Y_s). The measurement matrix Φ_s and the single spectral measurement Y_s were input into the FISTA program to reconstruct the millimeter-wave beam, shown in Fig. 6.3(b). It has the characteristic Gaussian beam profile one would expect.

6.3.3 Imaging Moving Targets

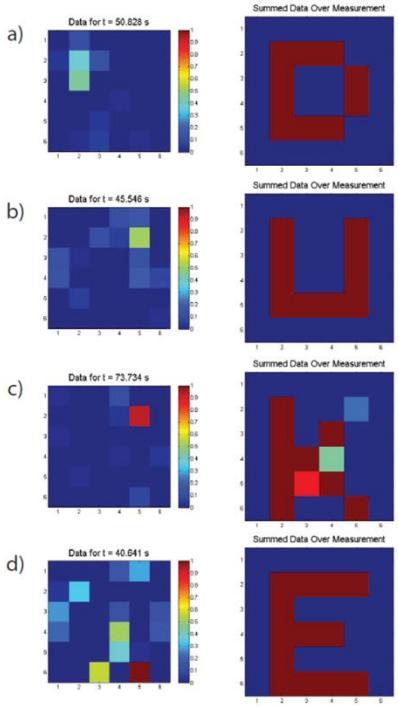

Fig. 6.4 – Imaging a Moving Object Still frames from movies tracking a moving pinhole at 6 fps. Each movie spells out a letter in the word "DUKE". The image on the left shows the reconstruction for that frame (a single pinhole) and the reconstruction on the right shows the summed data for each frame converted to a binary image. The stills shown in the figure are at the end of the motion path, after the letter has been spelled out. See Movies6.1.1 – 6.1.4.

As the measurements for Y_s are no longer serial in time, the image acquisition time can be greatly decreased over previous single camera architectures. In fact, we were able to sample images at approximately 6 fps ($\sim$150 ms/image). It is pertinent to note that this frame rate is

currently a limitation of the data acquisition software, and with some engineering could be optimized further. In Fig. 6.4 we show results from these measurements, where we have tracked the motion of a pinhole as it traverses the FOV on the mechanical XY stage at a speed of approximately 2.8mm/s (approximately 0.4 s/pixel). The left panel shows the reconstruction for the current frame, and the right panel shows the accumulated data over the course of the whole measurement, where each frame was made binary before being added to the accumulated image.

6.4 Conclusion

Here we have shown that by using *frequency* rather than *time* to encode measurements to a single pixel detector, we can increase the frame rate by a factor of 6 (and possibly even more with additional work on the data acquisition program). In the next chapter we will show additional ways in which image acquisition time can be reduced for a single pixel imaging system. In doing this, we still gain all the benefits of a single pixel detector (simplicity, sensitivity) while overcoming the time constraints.

7. Application of Telecommunication Techniques for THz Single Pixel Imaging

7.1 Introduction

As we have shown throughout this thesis, traditional single pixel imaging schemes multiplex a scene spatially in time, collecting serial measurements and reconstructing the image with post processing [92]. We noted in chapter 4 that this has the undesirable result that an increase in image resolution will require more masks and hence a slower image acquisition time. While applications of compressive sensing techniques [92, 103] have eased this restriction by reducing the number of spatial patterns needed to reconstruct a scene, the acquisition process is still generally serial in nature.

In this chapter, we utilize classic communication techniques in novel ways to decrease image acquisition time by increasing the number of parallel channels in which to encode information, allowing multiple mask patterns to be displayed simultaneously, rather than each one serially, hence reducing the total image acquisition time by some factor. We do this by encoding patterns on multiple carrier frequencies combined into a single, mixed frequency signal. Using standard phase sensitive detectors we can demodulate the detected signal, similar to the communications technique of frequency division multiplexing (FDM) [100]. Additionally, we can utilize the phase offset of our input signal with respect to a reference signal to implement quadrature amplitude modulation (QAM) [127] and access the full space of each carrier wave frequency. Combining FDM and QAM, we have access to 8 parallel channels and could thus reduce image acquisition time by a factor of 8. We show a proof-of-concept imaging experiment with QAM that easily reduces the image acquisition time by a factor of 2 and with FDM that reduces image acquisition time by a factor of 4 without significant loss of information.

7.2 Theory

Figure 7.1a shows a schematic of a traditional single pixel imaging system in which light from a scene passes through an active spatial light modulator. Our experimental apparatus is identical to the one used in chapter 5. Typically, patterns are displayed sequentially in time with a single measurement taken for each mask pattern. As the SLM plane is a conjugate image plane, mask patterns will spatially modulate the image and the measured values can be post-processed to reconstruct the scene. Below we will explain the mechanism in which we are able to encode masks simultaneously.

7.2.1 Signal Modulation and Lock-In Detection

Lock-in amplifiers (LIAs) are able to extract a small AC signal embedded in a large amount of noise and are especially useful in THz imaging set ups with low source power and strong atmospheric attenuation. The LIA houses a phase sensitive detector (PSD) that evaluates the relationship between the detected AC signal and a reference signal. In the case of our imaging set up, we modulate the SLM pixels at some frequency (a square wave into each pixel) and feed that same square wave into the LIA. Our THz detector outputs the signal summed from all the pixels on the SLM into the LIA, which in turn outputs a DC amplitude (V_0) and phase (θ) with respect to the reference signal or, alternatively X and Y components with $X = V_0\cos(\theta)$ and $Y = V_0\sin(\theta)$. In the first implementation of this imaging system, the phase of the input signal into the SLM was utilized to achieve [-1, 1] pixel values rather than the classic [0, 1] values associated with most SLMs [78].

7.2.2 Quadrature Amplitude Modulation

The modulation scheme above, accessing the $\theta = 0°$ and $\theta = 180°$ states, is known as binary phase-shift keying (BPSK). One can access not only $\theta = 0°$ and $\theta = 180°$ for *X* and *Y*, but also implement quadrature phase-shift keying (QPSK) in which combinations of *X* and *Y* are

achieved ($\theta = 45°, 135°, -135°, -45°$), giving access to 8 independent states on 2 orthogonal channels [128]. By tuning the phase of the input signal with respect to the reference signal, one can access the full *XY* space. We can also have amplitude shift keying (ASK), where we modulate the amplitude of 2 waves relative to one another. Modulating both amplitude and phase of 2 orthogonal channels is known as quadrature amplitude modulation (QAM) [127]. An example of this is 8QAM, where 8 phases around the XY plane are utilized and the amplitude of the *X*, *Y* signals is either 0 or 1.

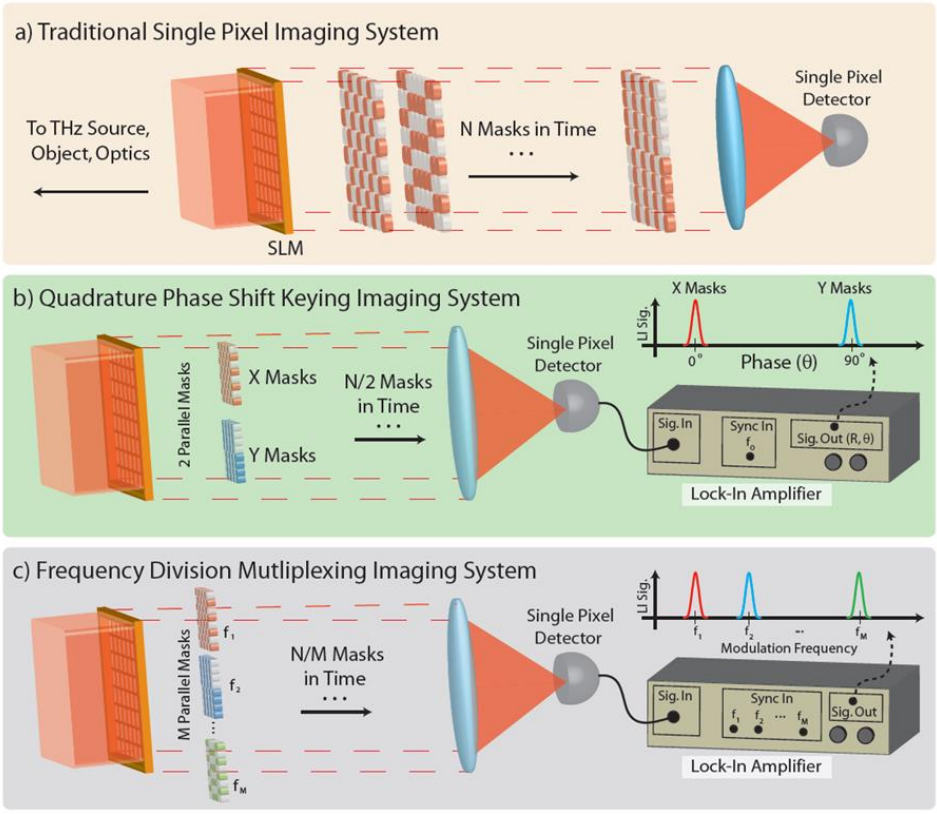

Fig. 7.1 – Imaging with Telecommunication Techniques (a) Conceptual schematic of a traditional single pixel imaging system. Masks are encoded in time and measured serially. (b) Single pixel imaging system using Quadrature Phase Shift Keying. Masks are encoded 2 at a time through the use of phase shift keying, and can be read through the *X* and *Y* component of the signal. This reduces the image acquisition time by a factor of 2. (c) Single pixel imaging system using Frequency Division Multiplexing. Masks can be encoded simultaneously and read out by looking at the Fourier Transformed signal for that modulation frequency. This reduces the image acquisition time by a factor of *M*.

Fig. 7.1(b) shows how imaging with QPSK can reduce the number of displayed masks by a factor of 2. For each frame, a mask is encoded in both *X* and *Y* (orthogonal channels on the LIA). The resulting signals are easily read and can be post-processed to separate masks. Fig. 7.2(a) shows the states for a QPSK encoding scheme. The red square wave is phase offset from the reference (black) to give access to 4 different states. These are plotted on a constellation diagram.

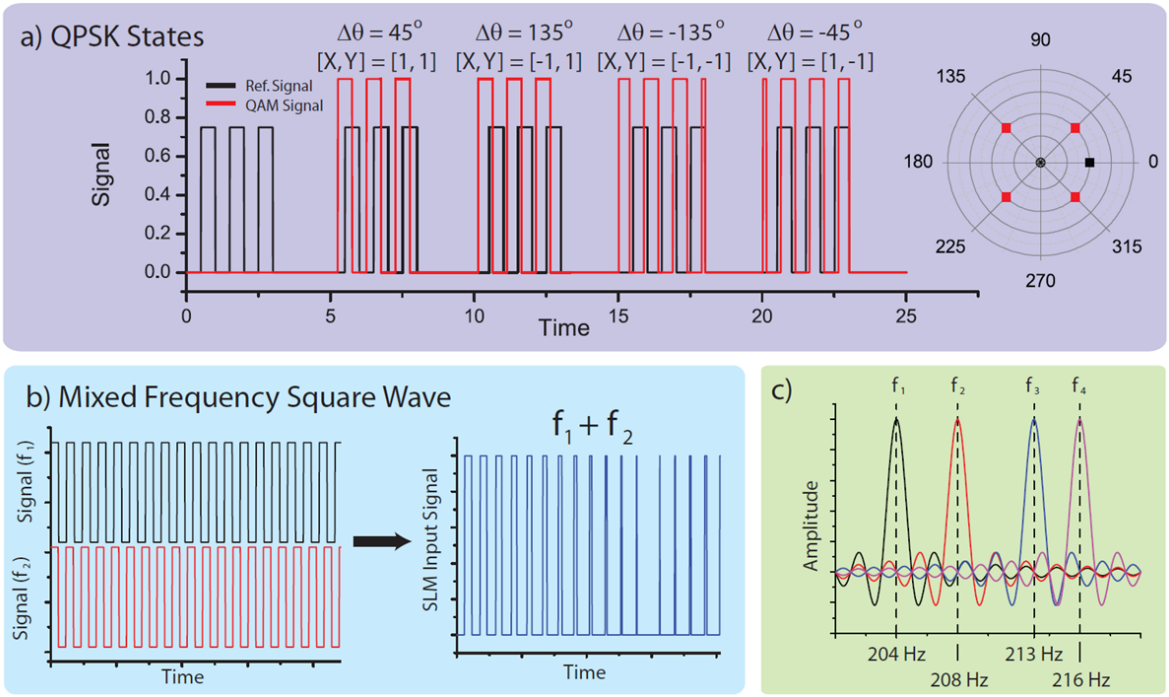

Fig. 7.2 – QAM and OFDM Signals Input signals for OFDM and QPSK. (a) Example states for QPSK. The 4 states are taken from the reference point (black square wave, at 0°). (b) Input signal example for 2 frequencies; a mixed frequency square wave is shown. (c) Fourier transform of 4 example OFDM frequencies. Note that the maxima of one occurs at the zero points of all the others.

7.2.3 Frequency Division Multiplexing

One of the benefits of using a LIA detection scheme is that the high-quality filter attenuates any other AC signal not at the reference frequency or a harmonic. Here we have exploited this to encode *multiple signals simultaneously*, each in a separate carrier frequency, with the total signal sent to several LIAs, each referenced to a separate subcarrier frequency. This

is similar to the standard communications concept of frequency division multiplexing (FDM), in practice since the late 1800's [129]. In FDM systems, the total bandwidth of the system is divided into several frequency bands, each of which carries a separate signal. The signals are combined on a single physical channel for transmission (a process known as modulation) and then separated after transmission (demodulation) [100].

FDM can be used for imaging by encoding different masks (i.e. rows of the measurement matrix Φ) onto each subcarrier. A mixed frequency square wave voltage will be applied to each pixel, with the amplitude and phase for each subcarrier frequency determined by the particular value for that mask and pixel. The LIA will then receive a summed signal for all the pixels with each mask in parallel encoded in different subcarriers. This is shown schematically in Fig. 7.1(c) where we see several masks being encoded simultaneously, reducing the overall image acquisition time. For example, if we encode masks on M carrier frequencies, we reduce the image acquisition time by a factor of M.

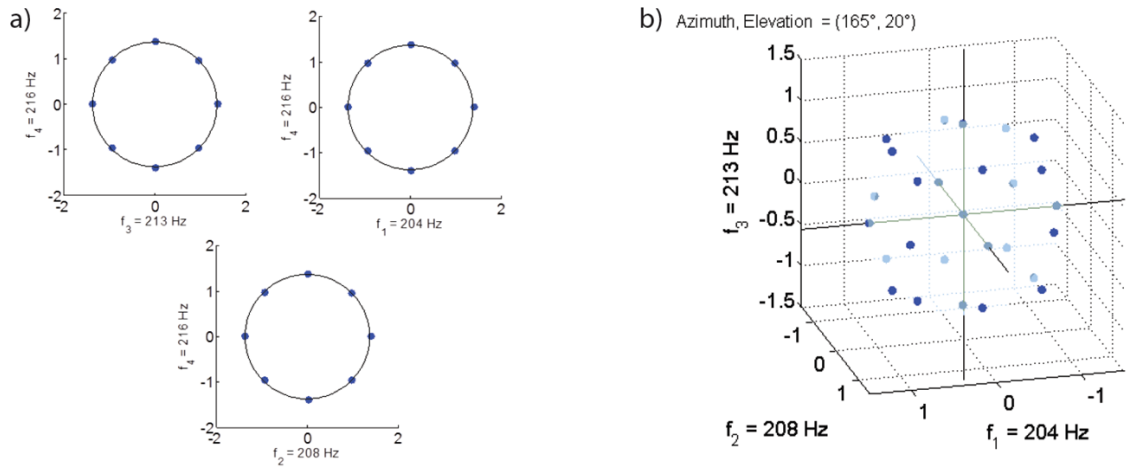

Fig. 7.3 – OFDM States All possible states for multi-frequency encoding (a) Constellation diagram for 2 frequencies plotted on a circle of the average radius for multiple different frequencies. (b) Constellation diagram for 3 frequencies plotted on a sphere of the average radius. See Movie 7.1.

In our implementation of FDM, the modulation occurs by combining several frequencies into a mixed frequency square wave (see Fig. 7.2(b)). The data is carried on a single channel (i.e. the THz radiation modulated by the SLM) to the detector.

7.2.4 Orthogonal Frequency Division Multiplexing

The choice of which modulation frequencies to use is not trivial and has a long history in the communications world. Here we choose orthogonal frequency division multiplexing (OFDM). The basic idea behind OFDM is to choose each subcarrier band such that its peak coincides with all other subcarrier's zero crossing points [130]. This can be seen in Fig. 7.2(c) where we show the frequency domain of the chosen subcarriers: f_1 = 204 Hz, f_2 = 208 Hz, f_3 = 213 Hz, f_4 = 216 Hz. The specific positioning of the subcarriers allows them to be spectrally orthogonal and gives optimal utilization of the available bandwidth [130].

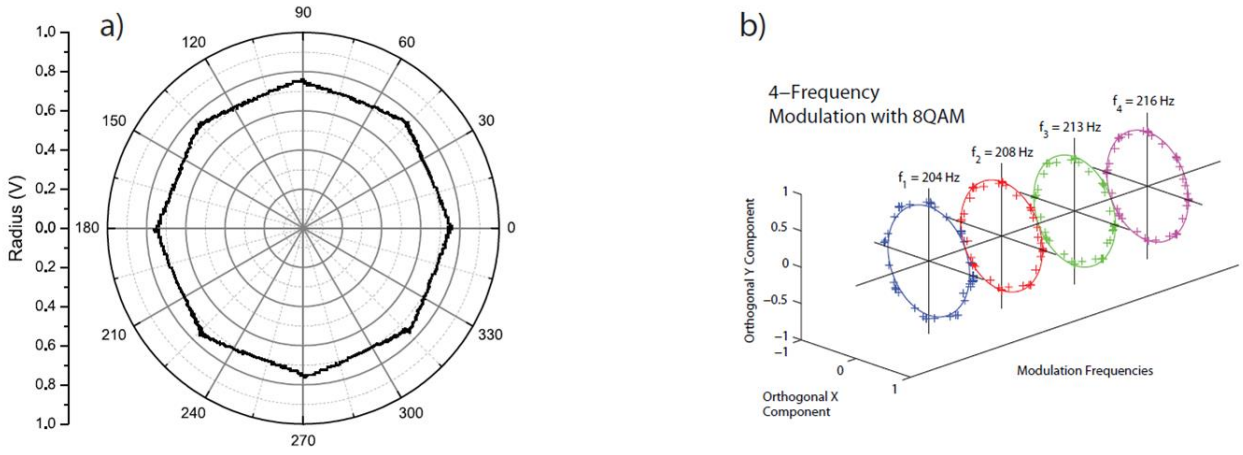

Fig. 7.4 – QAM and OFDM Encoding Simultaneous encoding of multi-frequency states with 8QAM. (d) 8 QAM constellation diagram. (e) 8 QAM constellation diagram for 4 frequencies encoded simultaneously. See Movie 7.2.

7.3 Results and Discussion

7.3.1 Possible states with FDM and QAM

Here we have demonstrated four-frequency modulation utilizing OFDM frequencies f_1 = 204Hz, f_2 = 208 Hz, f_3 = 213 Hz, f_4 = 216 Hz. Using the phase shift keying mentioned above, each frequency can attain one of 3 states: [1, 0, -1] and thus there are a total of 81 possible combinations ($[3\ \text{states}]^{[4\ \text{frequencies}]} = 81\ \text{independent states}$) implemented on 4 orthogonal channels. Constellation diagrams for these states are shown in Fig. 7.3. We can choose states that simultaneously modulate 1, 2, 3, or 4 frequencies. In Fig. 7.3(a) we show modulation of 2 simultaneous frequencies; the states lie on a circle of constant radius. In Fig. 7.3(b) we show modulation of 3 simultaneous frequencies; the states lie on a sphere of constant radius. This can be seen in Movie 7.1 where we rotate the sphere. Although it is not plotted, 4 simultaneous frequencies can be modulated independently and lie on the surface of a constant radius hypersphere.

In the above experiment, we have only utilized binary phase shift keying to access states ranging from [-1, +1] for each subcarrier. However, as explained above, each subcarrier can truly be represented as an amplitude and a phase with respect to the input reference signal for that subcarrier. Utilizing 8QAM gives us access to 4096 independent states (12 bits) on 8 orthogonal channels ($[8\ \text{states}]^{[4\ \text{frequencies}]} = 4096\ \text{independent states} = 12\ \text{bits}$). Fig. 7.4(b) shows the constellation diagram for a single frequency (f_4 = 216 Hz) where the *x* and *y* axes represent the orthogonal channels demodulated by the LIA. Fig. 7.4(b) shows all four subcarriers, each with the full 8QAM space mapped out. For each subcarrier, the *x* and *y* axes represent the *X* and *Y* output via the LIA while the z axis represents the modulation frequency. In addition, a multimedia file (Movie 7.2) shows a representation of raw data taken as a function of time. In the movie, several 8QAM states are accessed for each frequency simultaneously with little to no effect on the other frequencies, showing these channels are indeed orthogonal.

7.3.2 Imaging

As stated, the ability to not only phase shift key pixels to achieve [+1, -1] states, but also encode several masks simultaneously will have a large impact in image acquisition time. In fact, imaging masks encoded in *M* separate subcarriers will reduce the image acquisition time by a factor of *M*. Additionally, if each mask is implemented with QPSK, the image acquisition time could be reduced by a further factor of 2. Here we show two proof-of-concept imaging measurements.

One utilizes BPSK and QPSK to reduce the image acquisition time by a factor of 2. Fig 7.4f shows the BPSK reconstruction of a capital Greek letter sigma (Fig. 7.4(a)). The image acquisition time can be halved if we instead use QPSK, as has been done in Fig. 7.4(g). It is clear that the image retains its fidelity, even for the reduced image acquisition time.

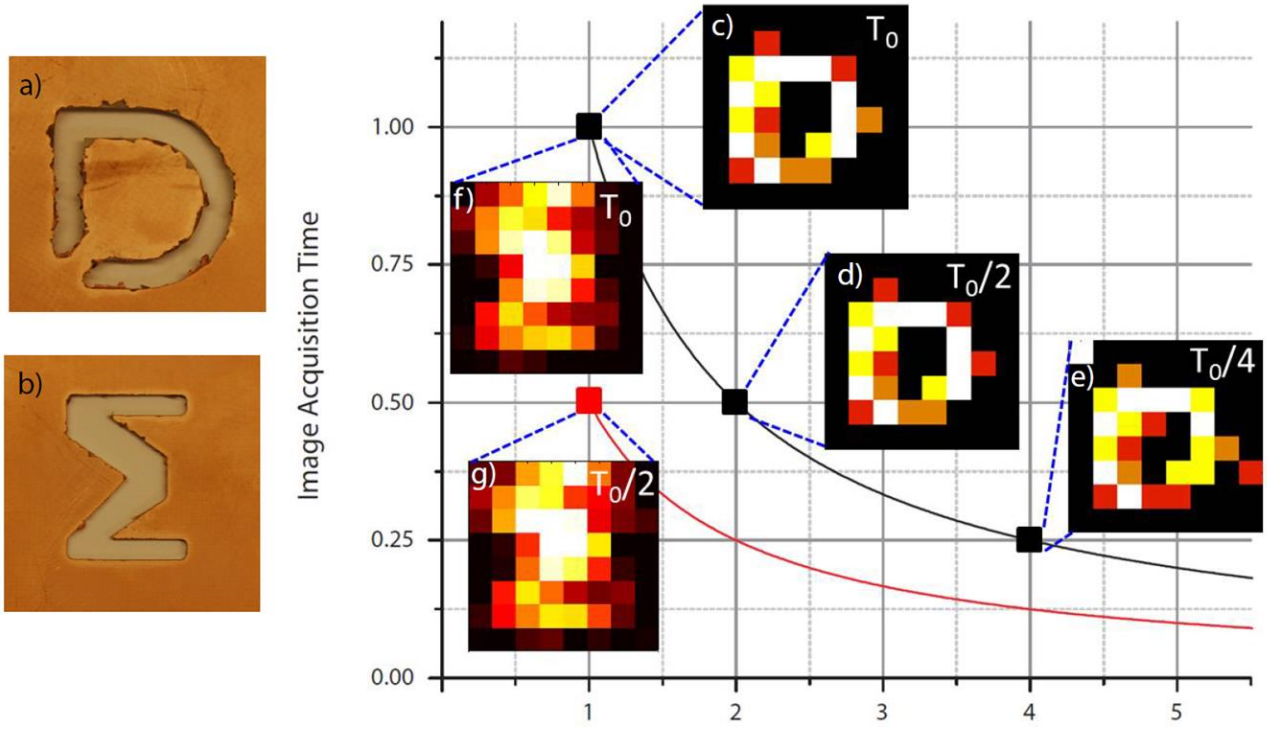

Fig. 7.5 – Imaging with QAM and OFDM (a) "D" aperture used for OFDM imaging. (b) "Σ" aperture used for QAM imaging. (c) Imaging using OFDM of one frequency (T_0), (d) 2 frequencies ($T_0/2$), and (e) 4 frequencies ($T_0/4$). (f) Imaging using BPSK (T_0) and (g) 4QAM ($T_0/2$).

The other experiment implements a binary phase shift keying over four subcarriers (OFDM frequencies f_1 = 204 Hz, f_2 = 208 Hz, f_3 = 213 Hz, f_4 = 216 Hz). Figure 7.4(a) shows the letter "D" milled into a metallic aperture which was imaged with optics onto the SLM. The figure shows reconstruction for a single frequency (f_1 = 204 Hz, Fig. 7.4(b)), 2 frequencies (f_1 = 204Hz, f_4 = 216 Hz, Fig. 7.4(c)), and all 4 OFDM subcarrier frequencies (Fig. 7.4(c)). The black trendline shows the $1/(\text{number of modulation frequencies})$ dependence of the image acquisition time. The red trendline shows the additional factor of 2 we gain through use of QPSK. It is clear from the figure that the image integrity is maintained while the masks are spread to double, and even quadruple the number of channels, while the image acquisition time drops accordingly.

7.4 Conclusion

In conclusion, we have shown a novel implementation of the classic telecommunication technique of OFDM. Implementing OFDM and 8QAM allows for 8 orthogonal channels in which to encode data. Not only have we demonstrated the ability to achieve any of these 4096 independent states, but we showed that they are indeed orthogonal. For single pixel imaging, this has the important effect of reducing the image acquisition time. We showed this in a proof-of-concept implementation with binary phase shift keying and 4 frequency modulation, reducing the image acquisition time by a factor of 4. Additionally, the demodulation scheme does not require any computationally heavy post-processing. Rather, data is sent to a standard lock-in amplifier, which accurately outputs data from the orthogonal channels. Possibly the most promising aspect of OFDM is that there is no need to stop at 4 frequencies; in fact, OFDM allows for the most optimal division of the available bandwidth. We could even go as far to implement the masks in 64 separate carrier frequencies, reducing the image acquisition time to the equivalent of a single

mask. These concepts have truly revolutionized the work described in chapter 5, and can be applied to any further projects that utilize a modulation-based detection scheme.

8. Conclusion and Future Outlook

This thesis laid out work that has been done over the past 5 years with efforts to study the physical phenomena behind metamaterials. Specifically, physical mechanism of metamaterial absorption and dynamic THz modulation were studied. These rich physical mechanisms can revolutionize long wavelength imaging. A comprehensive background has been given on the topic (chapters 1 – 3). Proof-of concept designs have been implemented in the THz and millimeter-wave regimes (chapters 4- 6). And in addition, techniques have been applied to make these systems more robust and efficient (chapter 7). There are still many techniques that can be applied to further the success of these imaging systems, some of which are listed below.

8.1 Photodoping Metamaterials for Efficient SLMs

In chapter 4 we discussed an active SLM in the THz regime using spatially photodoped silicon that gave a broadband tuning response. For many potential applications, it would be desirable to obtain spectral information, rather than integrating across a portion of the THz range. Metamaterials have shown an ability to modulate THz electromagnetic radiation with demonstrated advantages over conventional materials, including spectral selectivity, amplitude modulation [131], and phase modulation [38]. One could incorporate ρ –Si or another semiconductor into the MM design, in turn the photodoping would change the optical properties of the metamaterial as a whole [131].

The advantage in THz imaging provided by adding resonant metamaterials, is a potential increase in modulation depth at selected frequencies over bare silicon. The modulation depth could be further improved by optimizing the geometry of ρ -Si within the metamaterial unit cell, as well as the photodoping wavelength, both of which could potentially maximize the carrier density closer to the surface. Obtaining spectral information with conventional instruments can be

challenging, requiring complex high cost equipment and instrumentation with significantly limited acquisition speeds [132]. By arranging the pixels of metamaterial arrays to have uniquely designed operating frequencies we can create multi-color SLMs that could be used to perform high speed THz spectral imaging offering significant improvement over current systems. In addition, one could incorporate polarization sensitive masks, or phase-sensitive masks, to increase the flexibility of the MM-SLM.

8.2 Additional Techniques for Single Pixel Imaging

There are many additional techniques that can be implemented in single pixel imaging architectures. Some relate to the metamaterial design itself, such as encoding masks in different colors (i.e. response frequency of the metamaterial), using frequency information to identify certain objects, or implementing phase or polarization sensitive masks. In addition, one could explore things on a more mathematical end, such as changing the modulation levels of the mask (i.e. implement a non-binary system). Possibly the most exciting aspect of the designs laid out in this thesis and the techniques applied to them, is that they are all, much like metamaterials themselves, scalable to nearly any part of the electromagnetic spectrum.

8.3 Conclusions

In conclusion, metamaterials have physical phenomena that provide incredible insight into electromagnetic theory. In addition, their ability to manipulate light in the THz Gap has truly revolutionized imaging systems in long wavelength regimes. Their ability to maintain strong electromagnetic responses at frequencies typically inaccessible by natural materials has made them an ideal candidate for imaging devices. Combining efficient metamaterial devices with novel imaging techniques has pushed the single pixel imager from simply a proof-of-concept experiment, to a system with real-world applicability. This system will continue to be developed and has great potential for a multitude of purposes.

References

1. Maxwell, J. C., “A Dynamical Theory of the Electromagnetic Field,” *Royal Society Transactions* **155**, 459 – 512 (1865).
2. Jackson, J. D. *Classical Electrodynamics*. S.l.: John Wiley and Sons (WIE), 1998.
3. Kong, J. A. *Electromagnetic Wave Theory*. New York: Wiley, 1990.
4. Wiltshire, M. C. K. "Radio Frequency (RF) Metamaterials," *Physica Status Solidi (b)* **244**, 1227-236 (2007).
5. Alù, A. and Engheta, N., "Optical Nanotransmission Lines: Synthesis of Planar Left-handed Metamaterials in the Infrared and Visible Regimes," *Journal of the Optical Society of America B* **23**,571 (2006).
6. Bose, J. C., “On the rotation of plane of polarization of electric waves by a twisted structure,” *Proc. Roy. Soc.* **63**, 146 – 152 (1898).
7. Kock, W. E., "Metallic delay lenses," *Bell System Technical Journal* **27**, 58 – 82 (1948).
8. Schelhunoff, S. A. and Friis, H. T., “Antennas: Theory and Practice,” (John Wiley & Sons, New York, 1952).
9. Rotman, W., *IRE Trans. Antenna Prop.* **10**, 82 (1962).
10. Brown, J., “Artificial Dielectrics,” in *Progress in Dielectrics*, pg. 193 – 225 (Wiley, New York, 1960).
11. Pendry, J. B., *et al.*, "Magnetism from conductors and enhanced nonlinear phenomena," *Microwave Theory and Techniques, IEEE Transactions on* **47**, 2075 – 84 (1999).

12. Smith, D. R., *et al.*, "Composite medium with simultaneously negative permeability and permittivity," *Physical Review Letters* **84**, 4184 (2000).
13. Walser, R. M., "Electromagnetic metamaterials," *International Symposium on Optical Science and Technology*. International Society for Optics and Photonics, 2001.
14. Watts, C. M., X. Liu, and W. J. Padilla, "Metamaterial electromagnetic wave absorbers," *Advanced Materials* **24**, OP98 – OP120 (2012).
15. Liu, X., *et al.*, "Taming the blackbody with infrared metamaterials as selective thermal emitters," *Physical Review Letters* **107**, 045901 (2011).
16. Bingham, C. M., *et al.*, "Planar wallpaper group metamaterials for novel terahertz applications," *Optics Express* **16**, 18565-18575 (2008).
17. Chen, H.-T., *et al.*, "Active terahertz metamaterial devices," *Nature* **444**, 597-600 (2006).
18. Pendry, J. B., "Negative refraction makes a perfect lens," *Physical Review letters* **85**, 3966 (2000).
19. Schurig, D., *et al.*, "Metamaterial electromagnetic cloak at microwave frequencies," *Science* **314**, 977-980 (2006).
20. Shrekenhamer, D., *et al.*, "Four-Color Metamaterial Absorber THz Spatial Light Modulator," *Advanced Optical Materials* **1**, 905-909 (2013).
21. Capolino, F. *Theory and Phenomena of Metamaterials*. Boca Raton, FL: CRC/Taylor & Francis, 2009.
22. Veselago, V. G. "The Electrodynamics of Substances with Simultaneously Negative Values of ε and μ" *Physics-Uspekhi* **10**, 509-514 (1968).

23. Pendry, J. B., and D. R. Smith, "Reversing light with negative refraction," *Physics Today* **57**, 37-43 (2004).

24. Shelby, R. A., D. R. Smith, and S. Schultz, "Experimental verification of a negative index of refraction," *Science* **292**, 77-79 (2001).

25. Padilla, W. J., D. R. Smith, and D. N. Basov, "Spectroscopy of metamaterials from infrared to optical frequencies," *JOSA B* **23**, 404-414 (2006).

26. Chen, W-C., *et al.*, "Extremely subwavelength planar magnetic metamaterials," *Physical Review B* **85,** 201104 (2012).

27. Al-Naib, I. A., *et al.*, "Polarization and angle independent terahertz metamaterials with high Q-factors," *Applied Physics Letters* **98**, 091107 (2011).

28. Tao, H., *et al.*, "Highly flexible wide angle of incidence terahertz metamaterial absorber: Design, fabrication, and characterization," *Physical Review B* **78**, 241103 (2008).

29. O'brien, S., *et al.,* "Near-infrared photonic band gaps and nonlinear effects in negative magnetic metamaterials," *Physical Review B* **69**, 241101 (2004).

30. Xu, X., *et al.*, "Flexible visible–infrared metamaterials and their applications in highly sensitive chemical and biological sensing," *Nano Letters* **11**, 3232-3238 (2011).

31. Landy, N. I., *et al.*, "Perfect metamaterial absorber," *Physical Review Letters* **100,** 207402 (2008).

32. Armstrong, C. M. "THE TRUTH ABOUT TERAHERTZ," *IEEE Spectrum* **49**, 28 (2012).

33. Williams, G. P. "Filling the THz gap—high power sources and applications," *Reports on Progress in Physics* **69**, 301 (2006).

34. Cooper, K. B. *et al.*, "THz imaging radar for standoff personnel screening," *IEEE Trans. Terahertz Sci. Technol.* **1**, 169–182 (2011).

35. Goldsmith, P. F., Hsieh, C.-T., Huguenin, G. R., Kapitzy, J. & Moore, E. L., "Focal plane imaging systems for millimeter wavelengths," *IEEE Trans. Microwave Theory Technol.* **41**, 1664–1675 (1993).

36. Woodward, R. M. *et al.*, "Terahertz pulsed imaging of ex vivo basal cell carcinoma," *J. Invest. Dermatol.* **120**, 72–78 (2003).

37. Yen, T.-J., *et al.*, "Terahertz magnetic response from artificial materials," *Science* **303**, 1494-1496 (2004).

38. Chen, H.-T., *et al.*, "A metamaterial solid-state terahertz phase modulator," *Nature Photonics* **3,** 148-151 (2009).

39. O'Hara, J. F., *et al.*, "Thin-film sensing with planar terahertz metamaterials: sensitivity and limitations," *Optics Express* **16,** 1786-1795 (2008).

40. Xu, W., and S. Sonkusale, "Microwave diode switchable metamaterial reflector/absorber," *Applied Physics Letters* **103**, 031902 (2013).

41. Gil, I., *et al.*, "Tunable metamaterial transmission lines based on varactor-loaded split-ring resonators," *Microwave Theory and Techniques, IEEE Transactions on* **54**, 2665-2674 (2006).

42. Chen, H.-T., *et al.*, "Experimental demonstration of frequency-agile terahertz metamaterials," *Nature Photonics* **2**, 295-298 (2008).

43. Shrekenhamer, D., W.-C. Chen, and W. J. Padilla, "Liquid crystal tunable metamaterial absorber," *Physical Review Letters* **110**, 177403 (2013).

44. Tao, H., *et al.*, "Reconfigurable terahertz metamaterials," *Physical Review Letters* **103,** 147401 (2009).

45. CST Microwave Studio, https://www.cst.com.

46. Ansys HFSS, http://www.ansys.com.

47. Comsol Multiphysics, http://www.comsol.com.

48. Smith, D. R., *et al.*, "Electromagnetic parameter retrieval from inhomogeneous metamaterials," *Physical Review E* **71**, 036617 (2005).

49. Wang, B., T. Koschny, and C. M. Soukoulis, "Wide-angle and polarization-independent chiral metamaterial absorber," *Physical Review B* **80,** 033108 (2009).

50. Liu, N., *et al.*, "Infrared perfect absorber and its application as plasmonic sensor," *Nano Letters* **10**, 2342-2348 (2010).

51. Enkrich, C., *et al.*, "Focused-Ion-Beam Nanofabrication of Near-Infrared Magnetic Metamaterials," *Advanced Materials* **17,** 2547-2549 (2005).

52. Wu, C., *et al.*, "Large-area wide-angle spectrally selective plasmonic absorber," *Physical Review B* **84**, 075102 (2011).

53. Zhao, J., *et al.*, "Large-area high-quality plasmonic oligomers fabricated by angle-controlled colloidal nanolithography," *ACS Nano* **5,** 9009-9016 (2011).

54. Emerson, W.H. “Electromagnetic Wave Absorbers and Anechoic Chambers Through the Years,” *IEEE Trans. Antennas Propag.* **21** (4), July 1973.

55. Munk, B.A. “Frequency Selective Services,” (John Wiley and Sons, New York, 2000).

56. Knott, E.F., J.F. Shaeffer, and M.T. Tuley, "Radar Cross Section," 2nd ed., (SciTech Publishing, Raliegh, NC, 2004).

57. Popov, E., *et al.*, "Total Absorption of Un-polarized Light by Crossed Gratings," *Opt. Express* **16**, 6146–6155 (2008).

58. Knop, C.M., Y.B. Cheng, E.L. Ostertag, "An Absrober-Wall Parallel-Plate Waveguide," *IEEE Trans. Microwave Theory Tech.* **34** (7), 761–766 (1986).

59. Chou, R. S. Lee, "Modal Attenuation in Multilayered Coated Waveguides," *IEEE Trans. Microwave Theory Tech.* **36** (7), 1167–1176 (1988).

60. Namai, S. S., *et al.*, "Synthesis of an Electromagnetic Wave Absorber for High-Speed Wireless Communication," *J. Am. Chem. Soc.* **131**, 1170– 1173 (2009).

61. Tao, H. *et al.*, "A Metamaterial Absorber for the Terahertz Regime: Design, Fabrication, and Characterization," *Opt. Express* **16**, 7181–7188 (2008).

62. Liu, X., T. Starr, A. F. Starr, and W.J. Padilla, "Infrared Spatial and Frequency Selective Metamaterial with Near-Unity Absorbance," *Phys. Rev. Lett.* **104**, 207403 (2010).

63. Hao, J., *et al.*, "High Performance Optical Absorber Based on a Plasmonic Metamaterial," *Appl. Phys. Lett.* **96**, 251104 (2010).

64. Tao, H., *et al.*, "A Dual-Band Terahertz Metamaterial Absorber," *J. Phys. D. Appl. Phys.* **43**, 225102 (2010).

65. Shen, X., *et al.*, "Polarization-Independent Wide-Angle Triple-Band Metamaterial Absorber," *Opt. Express* **19**, 9401 (2011).

66. Alici, K. B *et al.*, "Optically thin composite resonant absorber at the near-infrared band: a polarization independent and spectrally broadband configuration," *Opt. Express* **19**, 14260 (2011).

67. Markos, P. and C.M. Soukoulis, "Wave Propagation," (Princeton UP, Princeton, NJ, 2008).

68. Born, M. and E. Wolf, "Principles of Optics," 7th ed. (Cambridge UP, New York, 1999).

69. Ordal, M. A. *et al.*, "Optical Properties of the metals Al, Co, Cu, Au, Fe, Pb, Ni, Pd, Pt, Ag, Ti, and W in the Infrared and Far Infrared," *Appl. Opt.* **22**, 1099–1120 (1983).

70. Eriksson, T.S., A. Hjortsberg, G.A. Niklasson, and C.G. Granqvist, "Infrared Optical Properties of Evaporated Alumina Films," *Appl. Opt.* **20** (15), 2742–2746 (1981).

71. Shamonina, E. and L. Solymar, "Properties of Magnetically Coupled Metamaterial Elements," *Journal of Magnetism and Magnetic Materials* **300** (1), 38–43 (2006).

72. Syms, R. R. A. and L. Solymar, "A Generic Approach to Boundary Reflection in Periodic Media," *The European Physical Journal B* **54**, 169–174 (2006).

73. Wiltshire, M. C. K., E. Shamonina, I.R. Young, and L. Solymar, "Dispersion Characteristics of Magneto-Inductive Waves: Comparison Between Theory and Experiment," *Electronics Letters* **39** (2), 215–217 (2003).

74. Gorkunov, M., M. Lapine, E. Shamonina, and K.H. Ringhofer, "Effective Magnetic Properties of a Composite Material with Circular Conductive Elements," *The European Physical Journal B* **28**, 263–269 (2002).

75. Lapine, M., *et al.*, "Structural Tunability in Metamaterials," *Appl. Phys. Lett.* **95**, 084105 (2009).

76. Sersic, I., M. Frimmer, E. Verhagen, and A.F. Koenderink, "Electric and Magnetic Dipole Coupling in Near-Infrared Split-Ring Metamaterial Arrays," *Phys. Rev. Lett.* **103**, 213902 (2009).

77. Powell, D., *et al.*, "Metamaterial Tuning by Manipulation of Near-Field Interaction," *Phys. Rev. B* **82**, 155128 (2010).

78. Watts, C. M., *et al.*, "Terahertz compressive imaging with metamaterial spatial light modulators," *Nat. Photon.* **8**, 605–609 (2014).

79. Withayachumnankul, W., *et al.*, "T-Ray Sensing and Imaging," *Proc. SPIE* **95**, 1528–1558 (2007).

80. Mittleman, D. M *et al.*, "Recent advances in terahertz imaging," *Appl. Phys. B* **68**, 1085–1094 (1999).

81. Chan, W. L., J. Deibel, and D. M. Mittleman, "Imaging with terahertz radiation," *Rep. on Prog. in Phys.* **70**, 1325–1379 (2007).

82. Korter, T. M. and D. F. Plusquellic, "Continuous-wave terahertz spectroscopy of biotin: vibrational anharmonicity in the far-infrared," *Chem. Phys. Lett.* **385**, 45–51 (2004).

83. Karpowicz, N. *et al.*, "Compact continuous-wave subterahertz system for inspection applications," *Appl. Phys. Lett.* **86**, 054105 (2005).

84. Kawase, K., Y. Ogawa, Y. Watanabe, and H. Inoue, "Non-destructive terahertz imaging of illicit drugs using spectral fingerprints," *Opt. Express* **11**, 2549 (2003).

85. Lee, A. W. and Q. Hu, "Real-time, continuous-wave terahertz imaging by use of a microbolometer focal-plane array," *Opt. Lett.* **30**, 2563–2565 (2005).

86. Butler, N. R. *et al.*, "Low-cost uncooled microbolometer imaging system for dual use," *Proc. SPIE* **2552** 583–591 (1995).

87. Wu, Q., T. D. Hewitt, and X. -C. Zhang, "Two-dimensional electro-optic imaging of THz beams," *Appl. Phys. Lett.* **69**, 1026–1028 (1996).

88. Hu, B. B. and M. C. Nuss, "Imaging with terahertz waves," *Opt. Lett.* **20**, 1716–1718 (1995).

89. Nuss, M. C. "Chemistry is right for T-ray imaging," *IEEE Circ. Dev. Mag.* **12**, 25–30 (1996).

90. Golay, M. J. E. Multi-Slit Spectrometry. Journ. Opt. Soc. Am. 39, 437 – 444 (1949).

91. Swift, R. D., Wattson, R. B., Decker, J. A., Paganetti, R. Jr. & Harwit, M. Hadamard transform imager and imaging spectrometer. *Appl. Opt.* **15**, 1595 – 1609 (1976).

92. Duarte, M. F. et al. Single-Pixel Imaging via Compressive Sampling. IEEE Sig. Proc. Mag. 25, 83 – 91 (2008).

93. Chan, W. L. et al. A single-pixel terahertz imaging system based on compressed sensing. Appl. Phys. Lett. 93, 121105 (2008).

94. Gopalsami, N. et al. Passive millimeter-wave imaging with compressive sensing. Opt. Eng. 51, 091614 (2012).

95. Chan, W. L. et al. A spatial light modulator for terahertz beams. Appl. Phys. Lett. 94, 213511 (2009).

96. Sensale-Rodriguez, B. et al. Terahertz imaging employing graphene modulator arrays. Opt. Exp. 21, 2324 – 2330 (2013).

97. Harwit, M. & Sloane, N. J. A. Hadamard Transform Optics. (Academic Press, New York, 1979).

98. Beer, T. Walsh transforms. Am. Phys. 49, 466 – 472 (1981).

99. Beauchamp, K. G. Applications of Walsh and Related Functions – With an Introduction to Sequency Theory. (Academic Press, New York, 1984).

100. Taylor, F. J. *Principles of Signals and Systems*. New York: McGraw-Hill, 1994.

101. Candès, E. J. and Wakin, M. B., "An Introduction to Compressive Sampling," IEEE Signal Processing Magazine 21 – 30 (March, 2008).

102. Donoho, D. L. et al. Data Compression and Harmonic Analysis. IEEE Trans. on Inf. Theory 44, 2435 (1998).

103. Donoho, D. L. Compressed Sensing. IEEE Trans. Inf. Theory 52, 1289 – 1306 (2006).

104. Candès, E. J. & Romberg, J. Robust Uncertainty Principles: Exact Signal Reconstruction from Highly Incomplete Frequency Information. IEEE Trans. Inf. Theory 52, 489 – 509 (2006).

105. Candès, E. J., Romberg, J. K. & Tao, T. Stable Signal Recovery from Incomplete and Inaccurate Measurements. Comm. on Pure and Appl. Math. LIX, 1207 – 1223 (2006).

106. Baranuik, R., Davenport, M., DeVore, R., & Wakin, M. A Simple Proof of the Restricted Isometry Property for Random Matrices. Constr. Approx. 28, 253 (2008).

107. Ganesh, A., Yang, A. Y. & Zhou, Z. (2010) SolveFISTA [Matlab R2011b]. Available at http://www.eecs.berkeley.edu/-yang/software/l1benchmark/.

108. Figueiredo, M., Nowak, R., and Wright S. (2007) SpaRSA [Matlab R2011b]. Available at www.lx.it.pt/~mtf/SpaRSA.

109. Candès, E. and Romberg, J. (2005) l_1-Magic [Matlab R2011b]. Available at http://users.ece.gatech.edu/~justin/l1magic/.

110. Bube, R.H. Photoelectronic Properties of Semiconductors, (Cambridge University, 1992).

111. Cooke, D. and P. U. Jepsen, "Optical modulation of terahertz pulses in a parallel plate waveguide," Opt. Express 16, 15123–15129 (2008).

112. Van Exter, M. and D. Grischkowsky, "Optical and electronic properties of doped silicon from 0.1 to 2 THz," Appl. Phys. Lett. 56, 1694–1696 (1990).

113. Alius, H. and G. Dodel, "Amplitude-, phase-, and frequency modulation of far-infrared radiation by optical excitation of silicon," Infrared Phys. 32, 1–11 (1991).

114. Jeon, T. and D. Grischkowsky, "Nature of conduction in doped silicon," Phys. Rev. Lett. 78, 1106–1109 (1997).

115. Schulenburg, H. and H. Tributsch, "Electropassivation of silicon and bulk lifetime determination with dry polymer contact," J. Phys. D 33, 851 (2000).

116. Hutley, C. Diffraction Gratings, (Academic, 1982).

117. Rice, J. P., J. E. Neira, M. Kehoe, and R. Swanson, "DMD diffraction measurements to support design of projectors for test and evaluation of multispectral and hyperspectral imaging sensors," Proc. SPIE 7210, 72100D (2009).

118. Bennet, C. A. Principles of Physical Optics (John Wiley & Sons, 2008).

119. Shirley, E. L. "Diffraction effects on broadband radiation: formulation for computing total irradiance," Appl. Opt. 43, 2609–2620 (2004).

120. Johnson, K. M., McKnight, D. J., & Underwood, I. Smart Spatial Light Modulators Using Liquid Crystals on Silicon. IEEE Journ. of Quant. Elec. 29, 699 – 714 (1993).

121. Chen, H.T. *et al.* Hybrid metamaterials enable fast electrical modulation of freely propagating terahertz waves. Appl. Phys. Lett. 93, 091117 (2008).

122. Davis, S. D. Multiplexed imaging by means of optically generated Kronecker products: 1. The basic concept. Appl.Opt. 34, 1170 – 1176 (1995).

123. Taylor, J. R. An Introduction to Error Analysis. (University Science, Sausalito, 1997).

124. Shrekenhamer, D., Watts, C. M., & Padilla, W. J. Terahertz single pixel imaging with an optically controlled dynamic spatial light modulator. Opt. Exp. 21, 12507 (2013).

125. Beck, A. & Teboulle, M. A. Fast-Iterative Shrinkage-Thresholding Algorithm for Linear Inverse Problems. SIAM Journal on Imaging Sciences 2, 183 – 202 (2009).

126. Schumann, S. et al. Spectrum to Space Transformed Fast Terahertz Imaging. Opt. Exp. 17, 19200 (2012).

127. Alencar, M. S., and V. C. da Rocha. "Quadrature Amplitude Modulation." *Communication Systems* (2005): 171-196.

128. Saadawi, T. N., M. H. Ammar, and A. E. Hakeem. *Fundamentals of Telecommunication Networks*. New York: Wiley, 1994.

129. Weinstein, S. B. "The history of orthogonal frequency-division multiplexing [History of Communications]." *Communications Magazine, IEEE*47.11 (2009): 26-35.

130. Wu, Y., and W. Y. Zou. "Orthogonal frequency division multiplexing: A multi-carrier modulation scheme." *Consumer Electronics, IEEE Transactions on* 41.3 (1995): 392-399.

131. Padilla, W. J., *et al.*, "Dynamical electric and magnetic metamaterial response at terahertz frequencies," Phys. Rev. Lett. 96, 107401 (2006).

132. DeVerse, R. A *et al.*, "Application of spatial light modulators for new modalities in spectrometry and imaging," Proc. SPIE 4959, 12–22 (2003).